nature portfolio

https://doi.org/10.1038/s41586-026-10768-1

Supplementary information

Nanocrystal-tailored recombination for all-perovskite tandem solar modules

In the format provided by the authors and unedited

Supplementary Information for

Nanocrystal-tailored recombination for all-perovskite tandem solar modules

Ke Xiao[1,2,3,10*], Hongfei Sun[1,10], Xinke Kong[4,10], Han Gao[1,10], Jing Lou[5], Xingze Chen[6], Zimo Hu[7], Dongdong Xu[1], Renxing Lin[1], Runnan Liu[1], Siyu Xia[4,8], Jin Xie[4,8], Ye Liu[2], Xin Luo[2], Fengjia Fan[7], Changqi Ma[6], Chao Chang[5], Yuanyuan Wang[4*]and Hairen Tan[1,2,9*]

[1]National Laboratory of Solid State Microstructures, College of Engineering and Applied Sciences, Frontiers Science Center for Critical Earth Material Cycling, Nanjing University, Nanjing 210023, China.

[2]Research and Development (R&D) Center, Renshine Solar (Suzhou) Co., Ltd., Suzhou, 215009, China

[3]School of Advanced Manufacturing Engineering, Nanjing University, Suzhou, China

[4]State Key Laboratory of Coordination Chemistry, School of Chemistry, Nanjing University, Nanjing 210023, China

[5]Innovation Laboratory of Terahertz Biophysics, National Innovation Institute of Defense Technology, Beijing, China.

[6]i-Lab & Printable Electronics Research Center, Suzhou Institute of Nano-Tech and Nano-Bionics, Chinese Academy of Sciences, Suzhou, 215123, China

[7]School of Physical Sciences, University of Science and Technology of China, Hefei, 230026, China.

[8]Jiangsu Key Laboratory of Advanced Organic Materials, Chemistry and Biomedicine Innovation Center (ChemBIC), Nanjing University, Nanjing, 210023, China.

[9] National Laboratory of Solid State Microstructures, College of Engineering and Applied Sciences, Jiangsu Physical Science Research Center, Nanjing University, Nanjing 210023, China

[10]These authors contributed equally to this work.

*Corresponding authors: ke.xiao@nju.edu.cn (K.X.); wangyy@nju.edu.cn (Y.W.); hairentan@nju.edu.cn (H.T.)

Contents

Supplementary Note 1. Tunnel recombination junction for all-perovskite tandem solar modules

This note provides a comparative analysis between the proposed solution-processed In_2O_3 NC recombination layer and the conventionally used sputtered ITO, specifically addressing their applicability in monolithic all-perovskite tandem solar modules. While sputtered ITO is a mature and effective material for small-area tandem cells, its implementation in large-area interconnected modules introduces a critical challenge related to the P2 interconnection structure. In monolithically interconnected tandem modules, the P2 channel directly exposes the recombination layer, creating a lateral electrical pathway between adjacent subcells. When the recombination layer exhibits high lateral conductivity, as is the case with sputtered ITO, this pathway can cause short-circuit between subcells, inducing leakage currents and reducing shunt resistance. This effect becomes increasingly pronounced as the module area increases, where longer P2 interconnection channels amplify lateral current leakage.

The solution-processed In_2O_3 NC layer is specifically designed to address this module-level limitation. Unlike sputtered ITO, which forms a dense and continuous conductive film, the In_2O_3 NC-based layer forms a nanocrystal-interconnected network with inherently limited lateral conductivity while preserving excellent vertical charge recombination. This anisotropic conductivity effectively suppresses P2-induced leakage pathways without compromising the vertical charge recombination required across the tunnel junction. Additionally, the solution processability of In_2O_3 NCs enables low-temperature deposition without sputtering-induced damage and provides a scalable route compatible with large-area coating processes.

To verify these advantages, we provide a direct experimental comparison between different recombination layers at both the cell and module levels, as shown in Supplementary Fig. 1. Our results demonstrate that while sputtered ITO performs adequately in small-area tandem cells (0.049 cm^2, Supplementary Fig. 1a and b), it leads to significant performance degradation in modules (65 cm^2) due to reduced shunt resistance and increased leakage current (Supplementary Fig. 1c). In contrast, the nanocrystal-based recombination layer effectively suppresses P2-induced shunting and maintains high module performance (Supplementary Fig. 1d). These results demonstrate that the In_2O_3-based recombination layer addresses a module-specific limitation of conventional sputtered TCOs, establishing its practical and scientific significance for high-performance all-perovskite tandem solar modules.

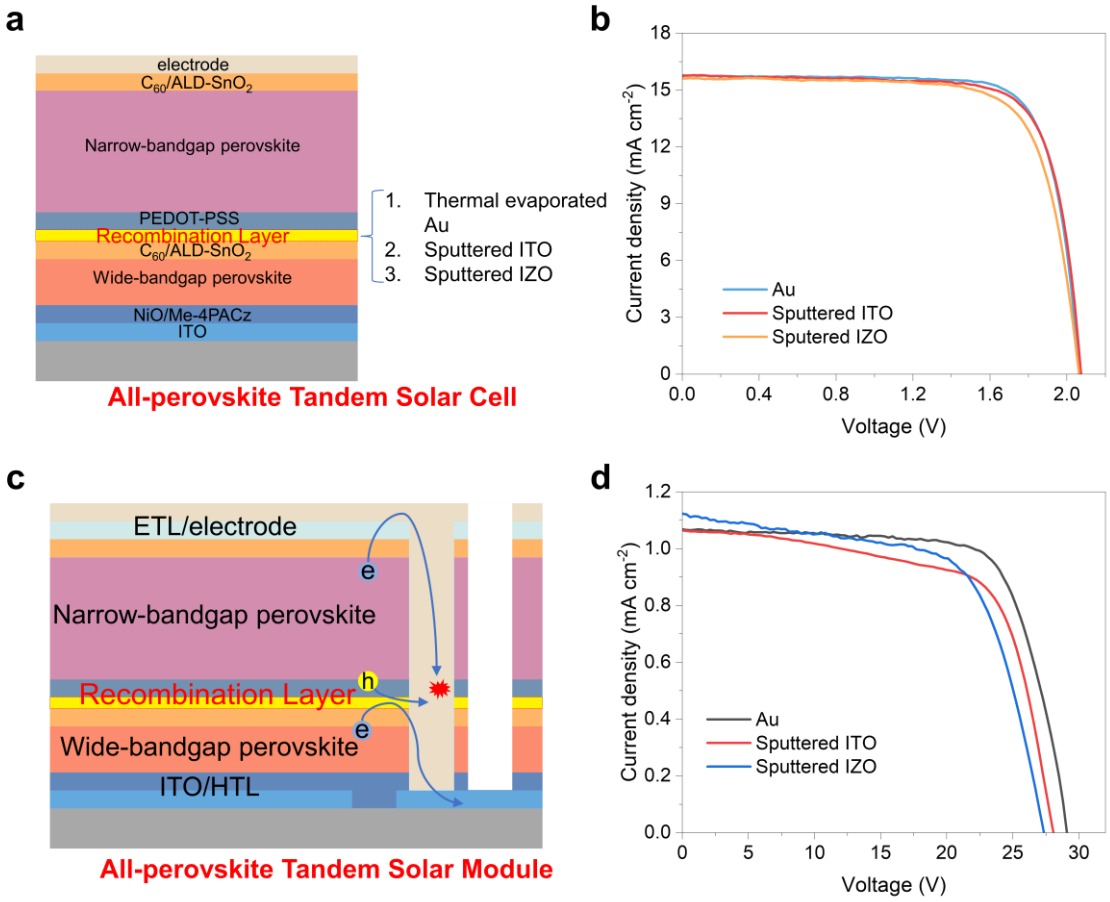

Supplementary Figure 1 | Photovoltaic performance of all-perovskite tandem solar cells and modules using different recombination layers. (a) Configuration diagram of tandem structure using different recombination layers; (b) J-V curves of the all-perovskite tandem solar cells using different recombination layers; (c) Configuration diagram of the shunting in tandem solar modules while using sputtered TCO as recombination layers; (d) J-V curves of the all-perovskite tandem solar modules using different recombination layers.

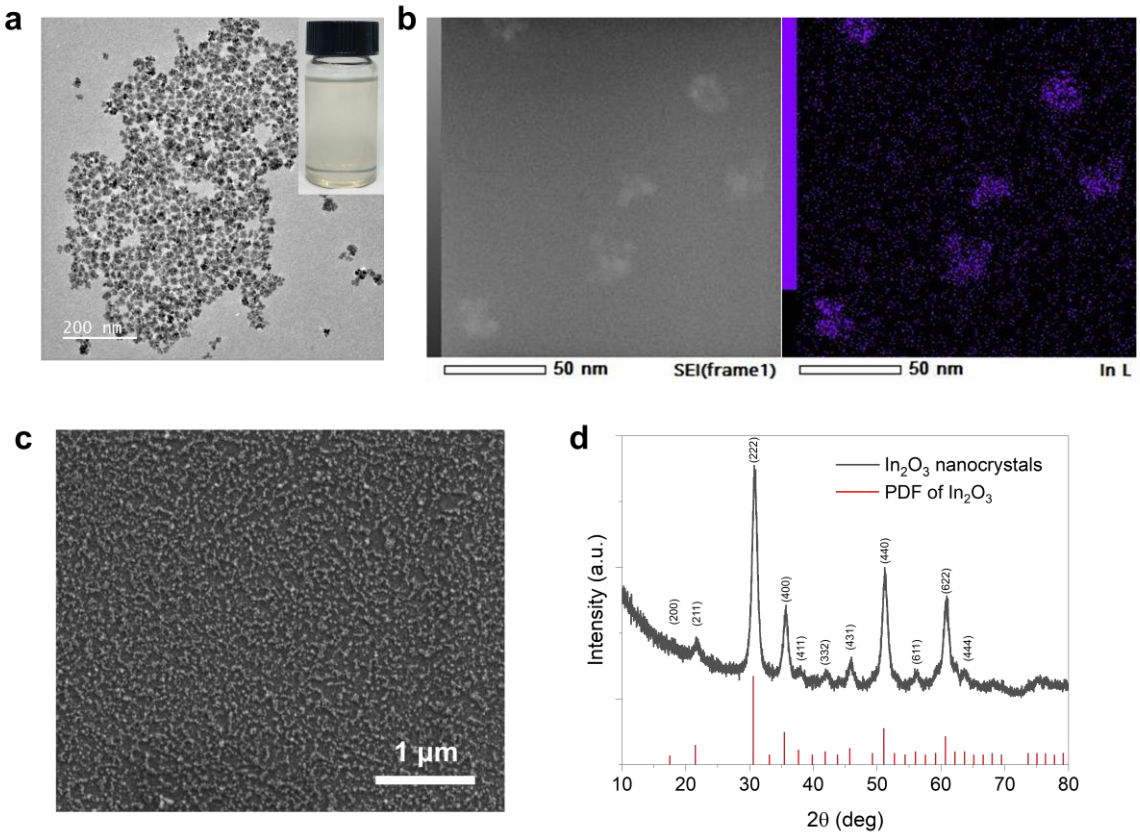

Supplementary Figure 2 | Synthesis of In_2O_3 nanocrystals. (a) TEM image of In_2O_3 nanocrystals. (b) HAADF-EDS of In_2O_3 nanocrystals. (c) SEM images of In_2O_3 nanocrystal films by blade-coated on the ITO substrate. (d) XRD pattern of In_2O_3 nanocrystals.

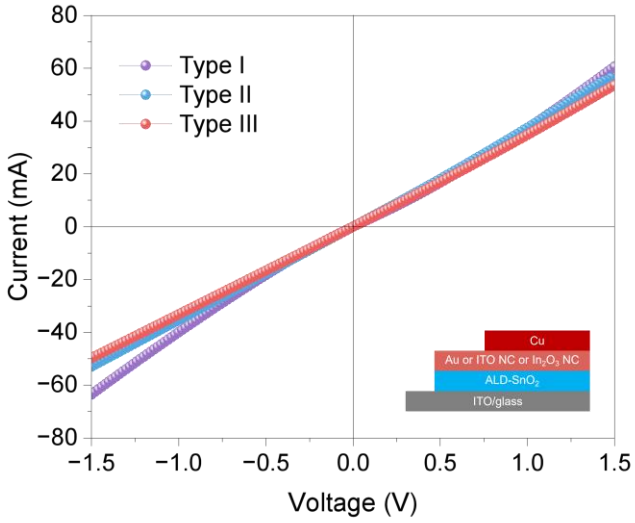

Supplementary Figure 3 | I-V curves of the TRJs with different recombination layers. Insert is the device structure.

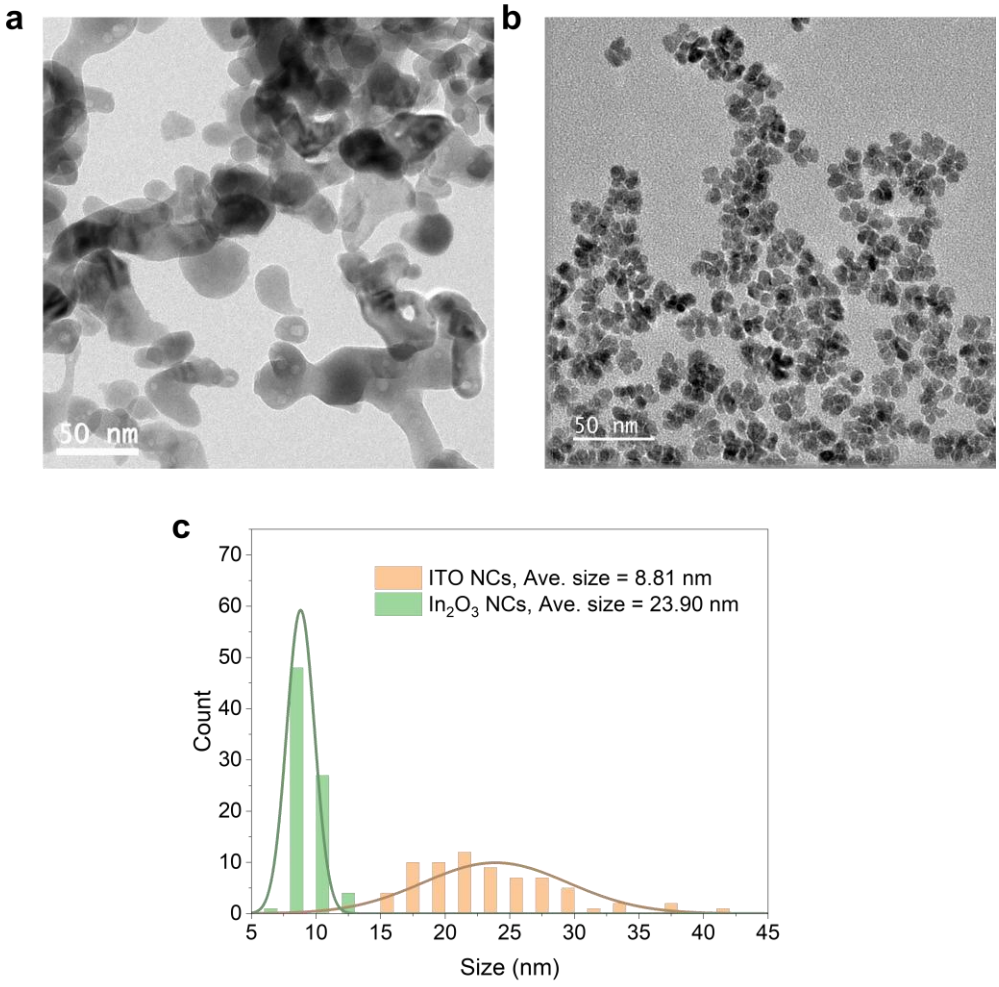

Supplementary Figure 4 | Morphology comparison of ITO and In_2O_3 NCs. (a) TEM image of purchased commercial ITO NCs. (b) TEM image of self-synthesized In_2O_3 NCs. (c) Particle size statistics of ITO and In_2O_3 NCs.

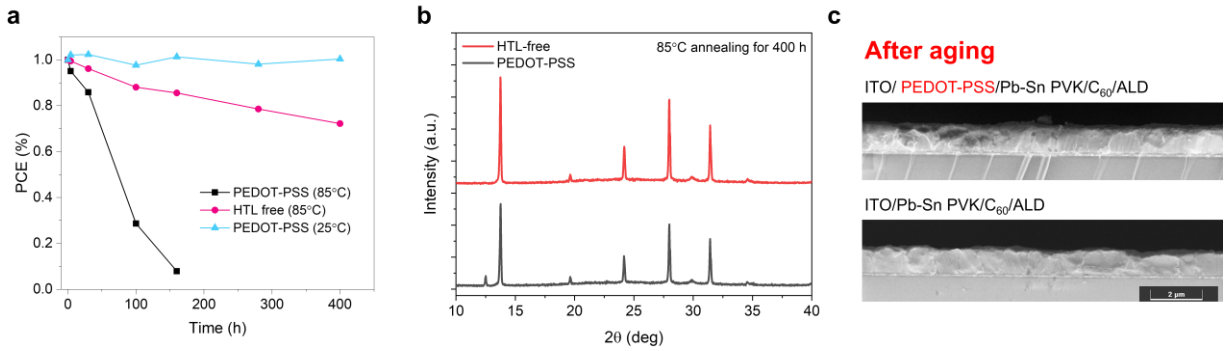

Supplementary Figure 5 | Thermal stability of the Pb-Sn PSCs. (a) Thermal stability tracking of the PEDOT-PSS-based and HTL-free Pb–Sn PSCs aged at 85 °C for 400 hours. (b) XRD patterns of the perovskite films on PEDOT-PSS or bare ITO after 400 hours of thermal aging. The film on PEDOT-PSS shows initial signs of degradation. (c) Cross-sectional SEM images of the PSCs with PEDOT-PSS or bare ITO after the 400-hour thermal aging test.

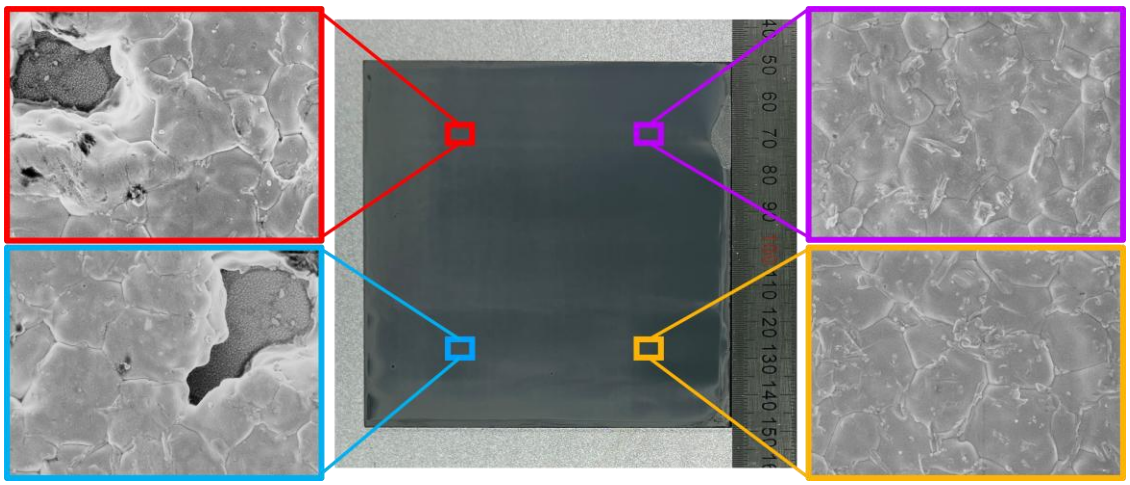

Supplementary Figure 6 | Digital photo and zoomed-in SEM images of the large-scale DMF:DMSO-based Pb-Sn perovskite film deposited on 10×10 cm^2 substrate while using an optimal coating speed of 3 mm/s. The perovskite film shows pinholes because of the slow nucleation, leading to ununiform crystallization.

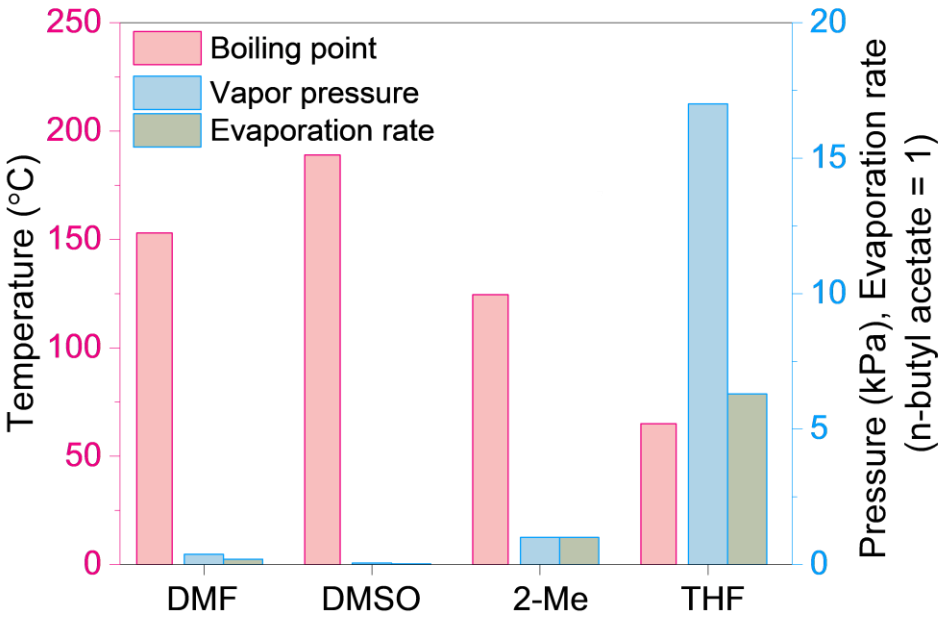

Supplementary Figure 7 | Boiling point, vapor pressure, and evaporation rate comparison of different solvents (eg. DMF, DMSO, 2-Me and THF).

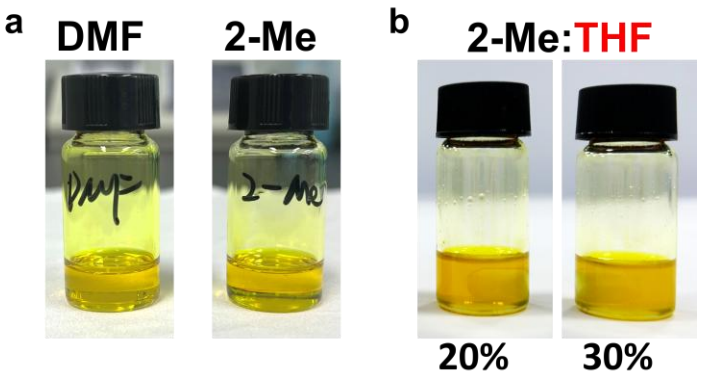

Supplementary Figure 8 | Solvent comparison for Pb-Sn perovskite. (a) Digital photos of the Pb-Sn perovskite precursor. Left is the Pb-Sn perovskite dissolved in DMF:DMSO with the concentration of 2.4M, right is the Pb-Sn perovskite dissolved in 2-Me with the concentration of 1.4M; (b) Digital photos of the Pb-Sn perovskite precursor using mixed 2-Me:THF. The volume ratios of THF are 20% (left) and 30% (right), respectively. Slight precipitate can be observed at 30%.

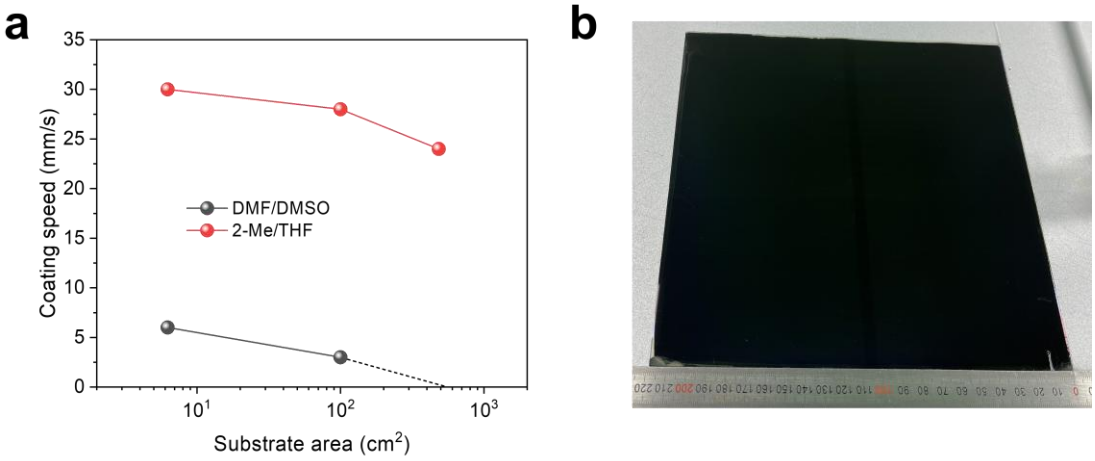

Supplementary Figure 9 | Large-area fabrication of Pb-Sn perovskite films. (a) The optimal coating speed using gas-assisted blade coating for different-sized substrates. (b) Target Pb-Sn perovskite using 2-Me:THF deposited on a 22×22 cm^2 substrate.

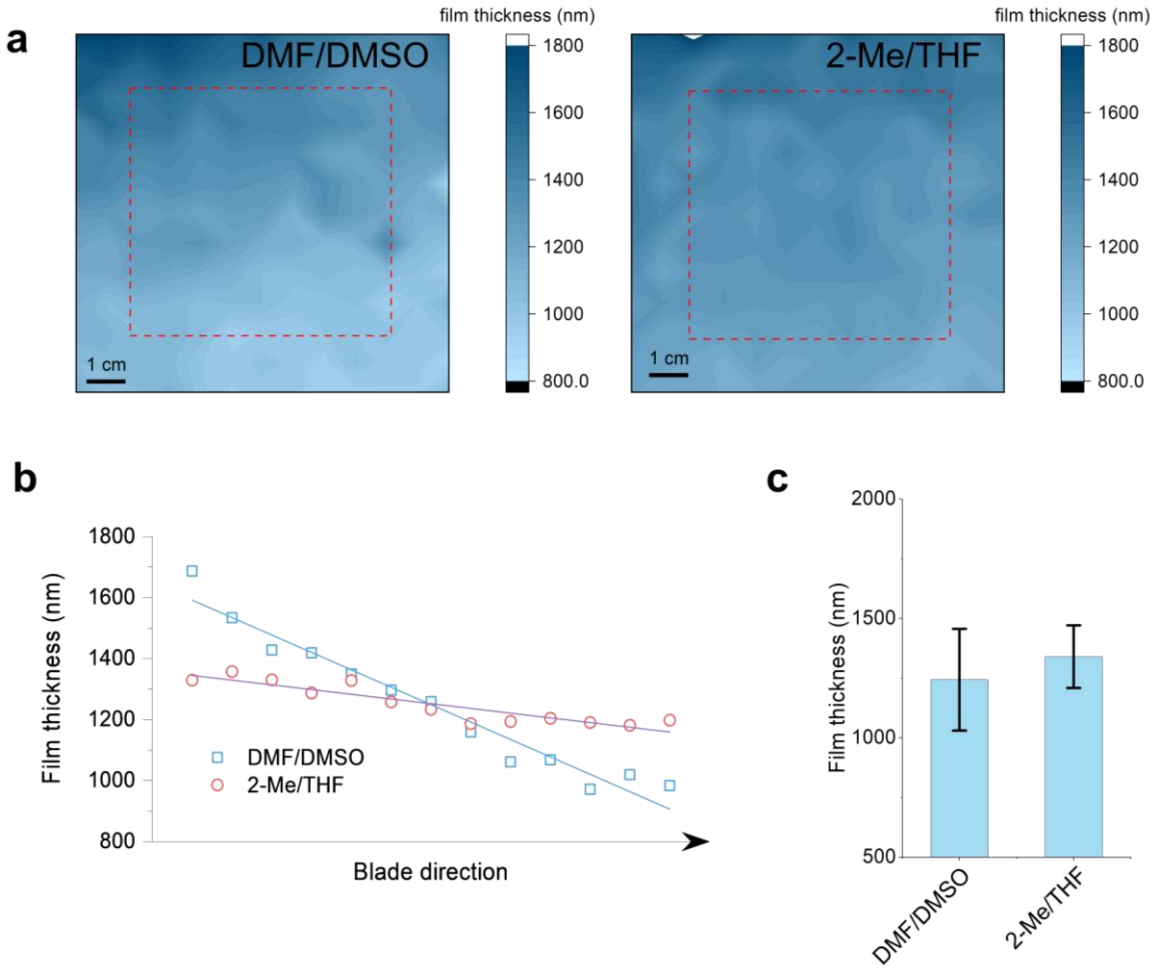

Supplementary Figure 10 | Film uniformity of the large-scale DMF-based and 2-Me-based Pb-Sn perovskite films. (a) Film thickness uniformity of the DMF-based and 2-Me-based Pb-Sn perovskite films; (b) Film thickness evolution along with the coating direction; (c) Statistics of perovskite film thickness deposited on 10×10 cm^2 substrate using DMF:DMSO and 2-Me:THF. The perovskite film based on 2-Me:THF exhibits better thickness uniformity than that based on DMF:DMSO.

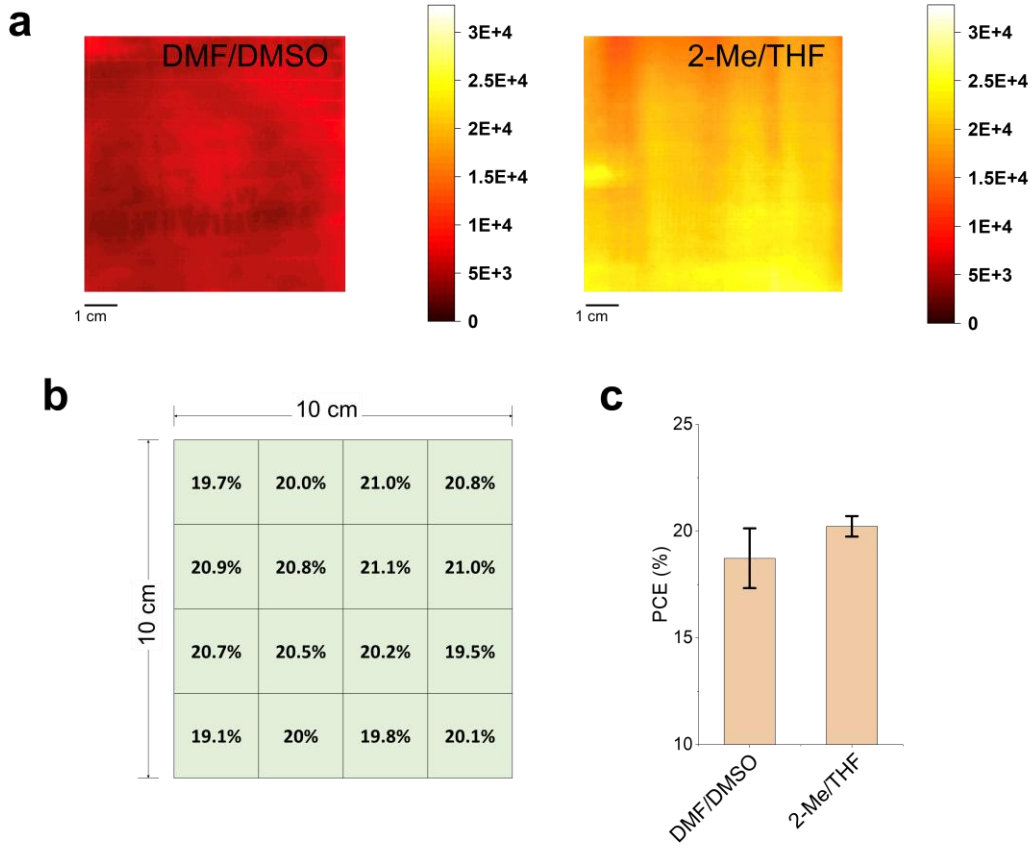

Supplementary Figure 11 | Optoelectrical uniformity of the large-scale DMF-based and 2-Me-based Pb-Sn perovskite films. (a) PL mapping images of DMF-based and 2-Me-based perovskite films of 8×8 cm^2 region at the center of 10×10 cm^2 substrates. (b) Different pixel efficiencies using 2-Me-based Pb-Sn perovskite within the 10×10 cm^2 substrate. (c) The efficiency uniformity of the PSCs from the 10×10 cm^2 substrate fabricated using 2-Me-based solvent is much better than those fabricated by DMF-based solvent. 16 devices from (b) with aperture area of 0.049 cm^2. The error bar represents the standard deviation.

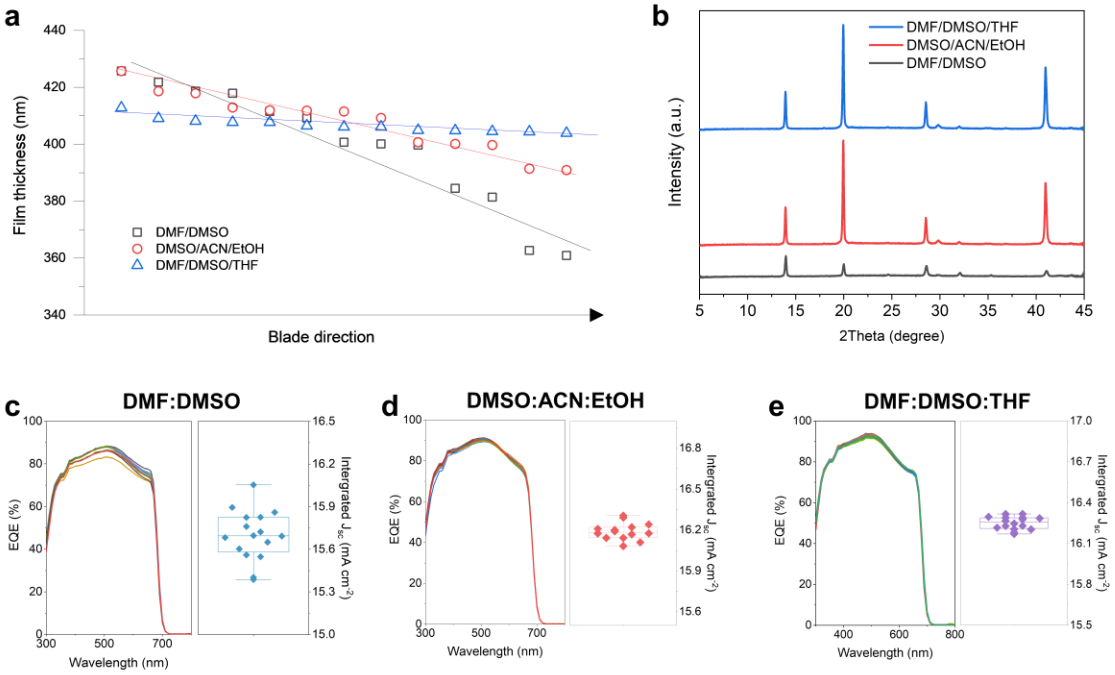

Supplementary Figure 12 | Comparison of different solvent systems. (a) Film thickness evolution along with the coating direction based on 10×10 cm^2 substrates. (b) XRD patterns of $Cs_{0.35}FA_{0.65}PbI_{1.8}Br_{1.2}$ wide-bandgap perovskite using different solvent systems. (c-e) EQE spectra and corresponding integrated J_{SC} of wide-bandgap topcell fabricated using different solvent systems in tandem solar modules. During this evaluation, however, the previously reported green solvent system [1] produced a noticeable thickness gradient across the substrate. We attribute this behavior to the relatively high DMSO fraction in the formulation, which slows solvent evaporation. Under large-area blade-coating conditions, where the surface-to-volume ratio decreases and the coating speed must be balanced with gas-assisted drying, the slower evaporation kinetics make it difficult to maintain uniform crystallization across the entire substrate.

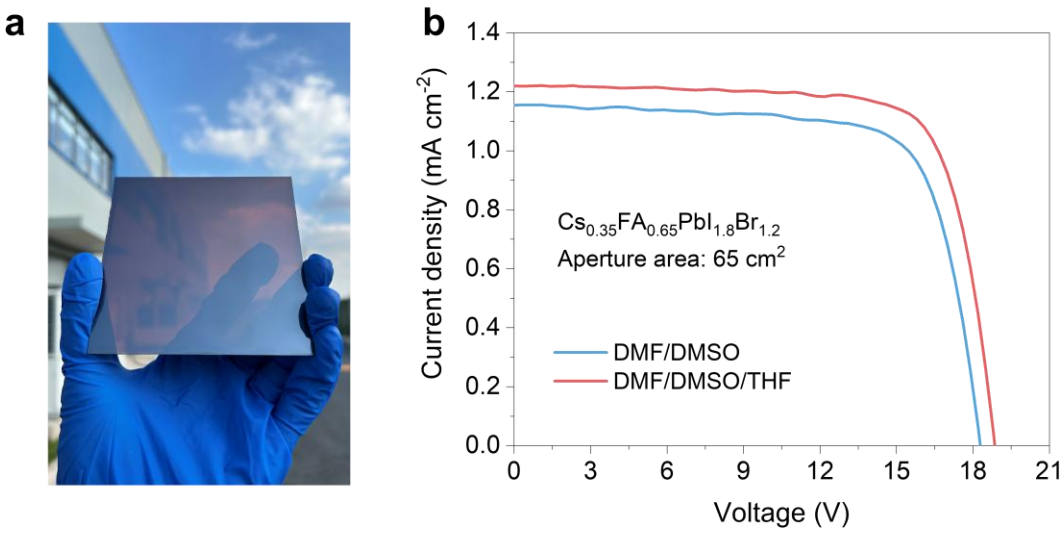

	V_{oc} (V)	J_{sc} (mA cm^{-2})	FF (%)	PCE (%)
DMF/DMSO	18.411	1.155	72.9	15.5
DMF/DMSO/THF	19.043	1.220	75.2	17.5

Supplementary Figure 13 | Large-scale fabrication of wide-bandgap perovskite solar modules. (a) Digital photos of a 10×10 cm^2 wide-bandgap perovskite film. (b) J-V curves of the best-performing single-junction wide-bandgap perovskite solar modules.

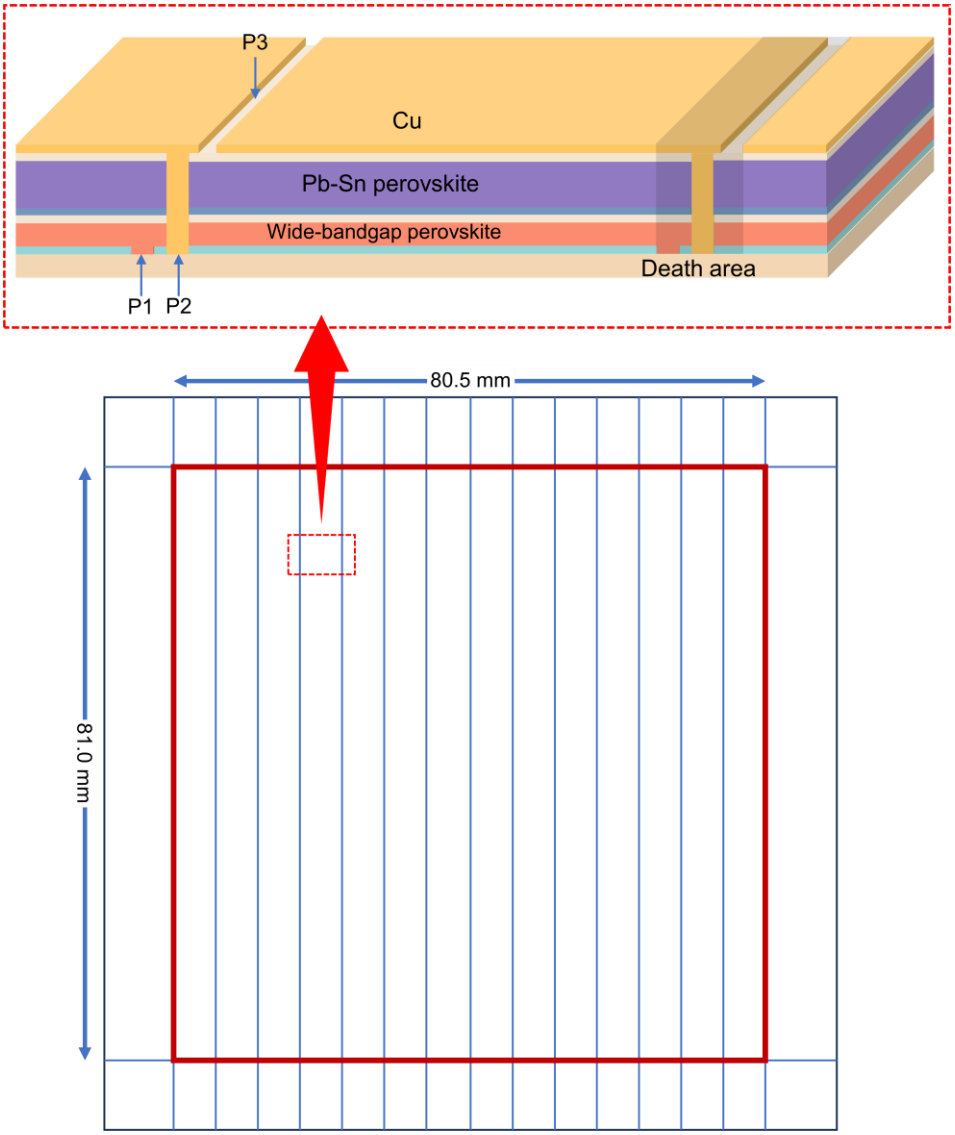

Supplementary Figure 14 | Schematic diagram of the series-connected all-perovskite TSM design and structure.

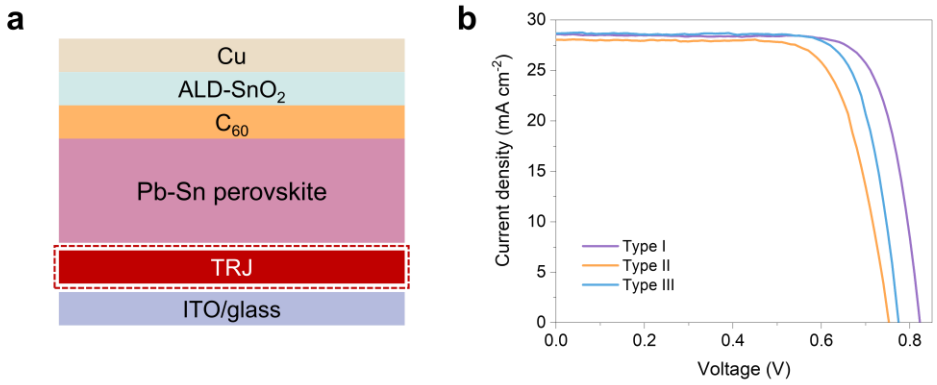

Supplementary Figure 15 | Pb-Sn perovskite single-junction solar cells. (a) Schematic diagram of the structure of the Pb-Sn perovskite single-junction solar cell using TRJ as HTL. (b) J-V curves of corresponding Pb-Sn PSCs using different TRJs as HTL.

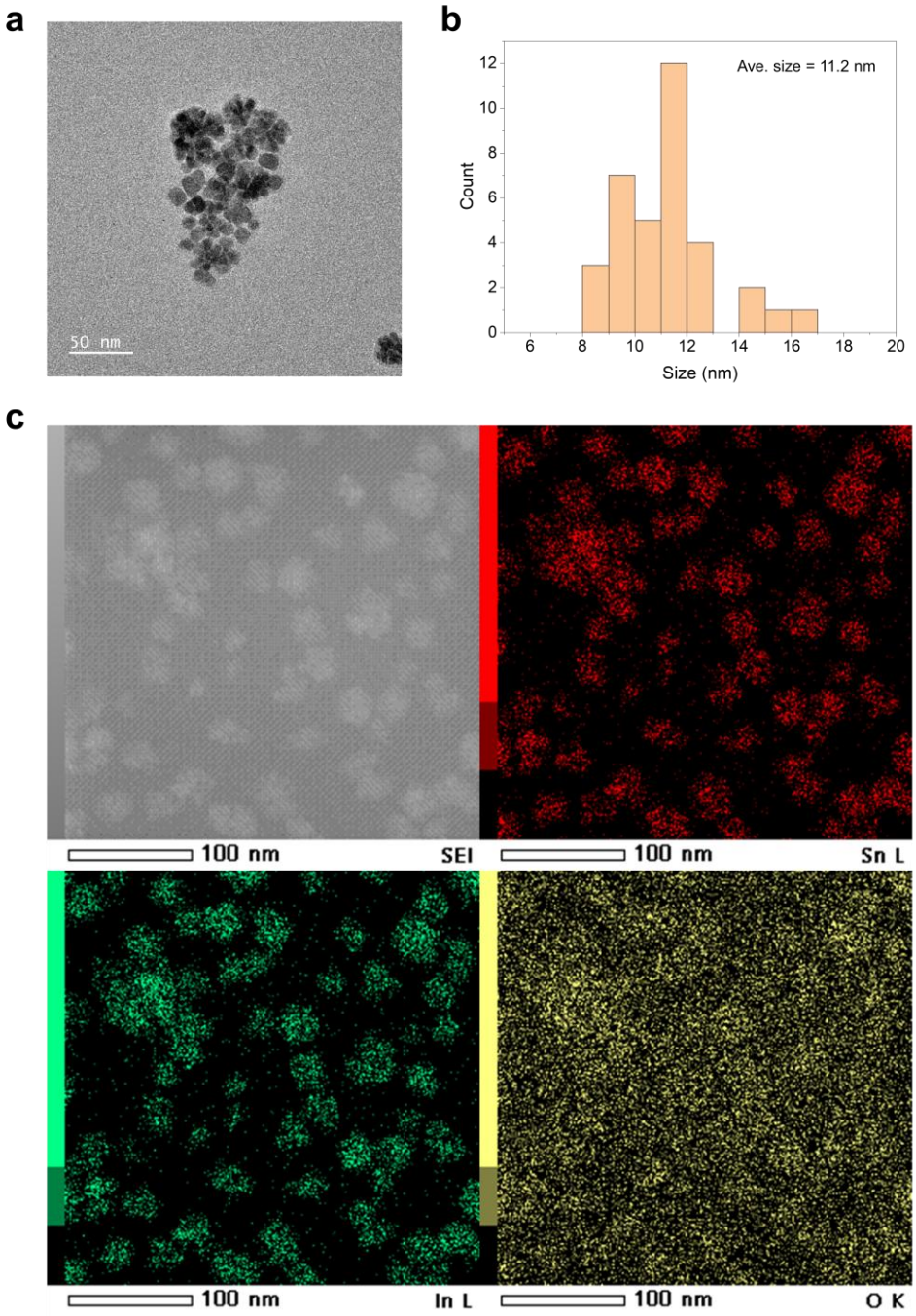

Supplementary Figure 16 | Synthesis of ITO NCs. (a) TEM image of the self-synthesized ITO NCs. (b) Particle size statistics of ITO NCs. (c) HAADF-EDS of ITO NCs.

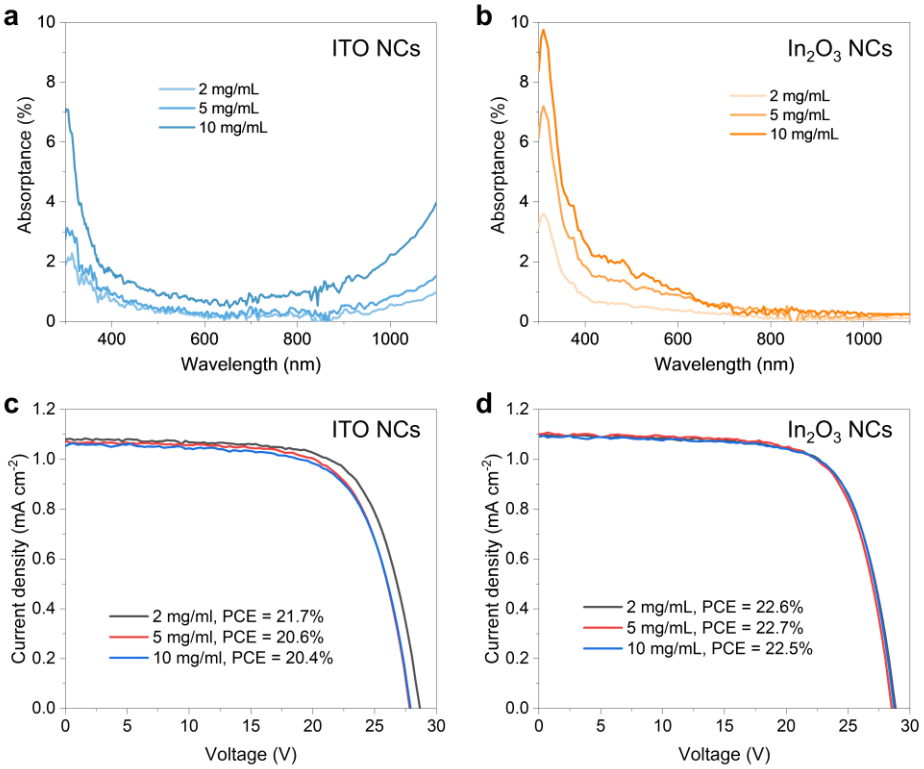

Supplementary Figure 17 | Optoelectrical property comparison. (a-b) Absorptance of different thickness of (a) ITO NCs and (b) In_2O_3 NCs using concentration from 2 mg/mL to 10 mg/mL. (c-d) Module performance comparison between ITO NCs and In_2O_3 NCs using concentration from 2 mg/mL to 10 mg/mL.

a

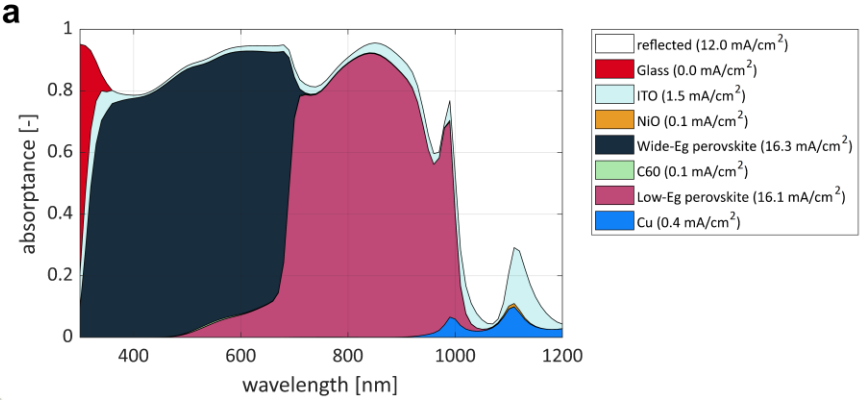

b

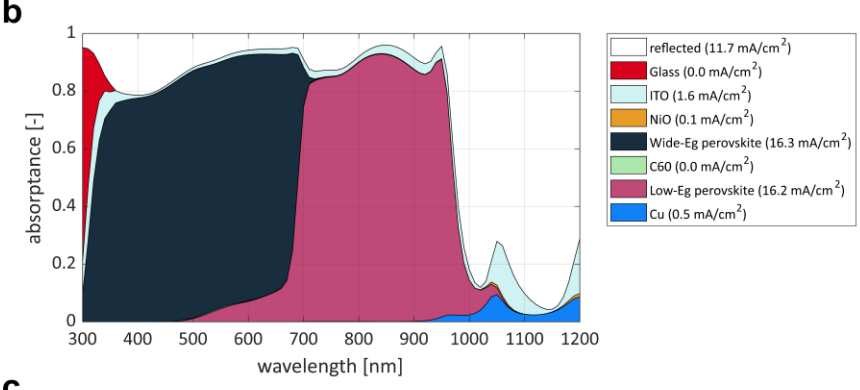

c

	ITO NC			In_2O_3 NC		
	10 nm	20 nm	30 nm	10 nm	20 nm	30 nm
J_{ph} of wide	16.31	16.32	16.32	16.31	16.32	16.32
J_{ph} of narrow	16.24	16.14	16.07	16.29	16.25	16.23

d

	Baseline	Extra roughness	Diff (%)	Baseline	Extra roughness	Diff (%)
	ITO NC = 10 nm	add extra texture		In_2O_3 NC = 10 nm	add extra texture	
J_{ph} of wide	16.31	16.31	-0.0059	16.31	16.31	-0.0059
J_{ph} of narrow	16.24	16.24	0.0040	16.29	16.30	0.0040

Supplementary Figure 18 | Optical simulations. Optical simulation of all-perovskite tandems using (a) 30-nm thickness of ITO NCs and (b) 10-nm thickness of In_2O_3 NCs. (c) Thickness sensitivity and (d) roughness sensitivity of all-perovskite tandems between ITO NCs and In_2O_3 NCs as recombination layer.

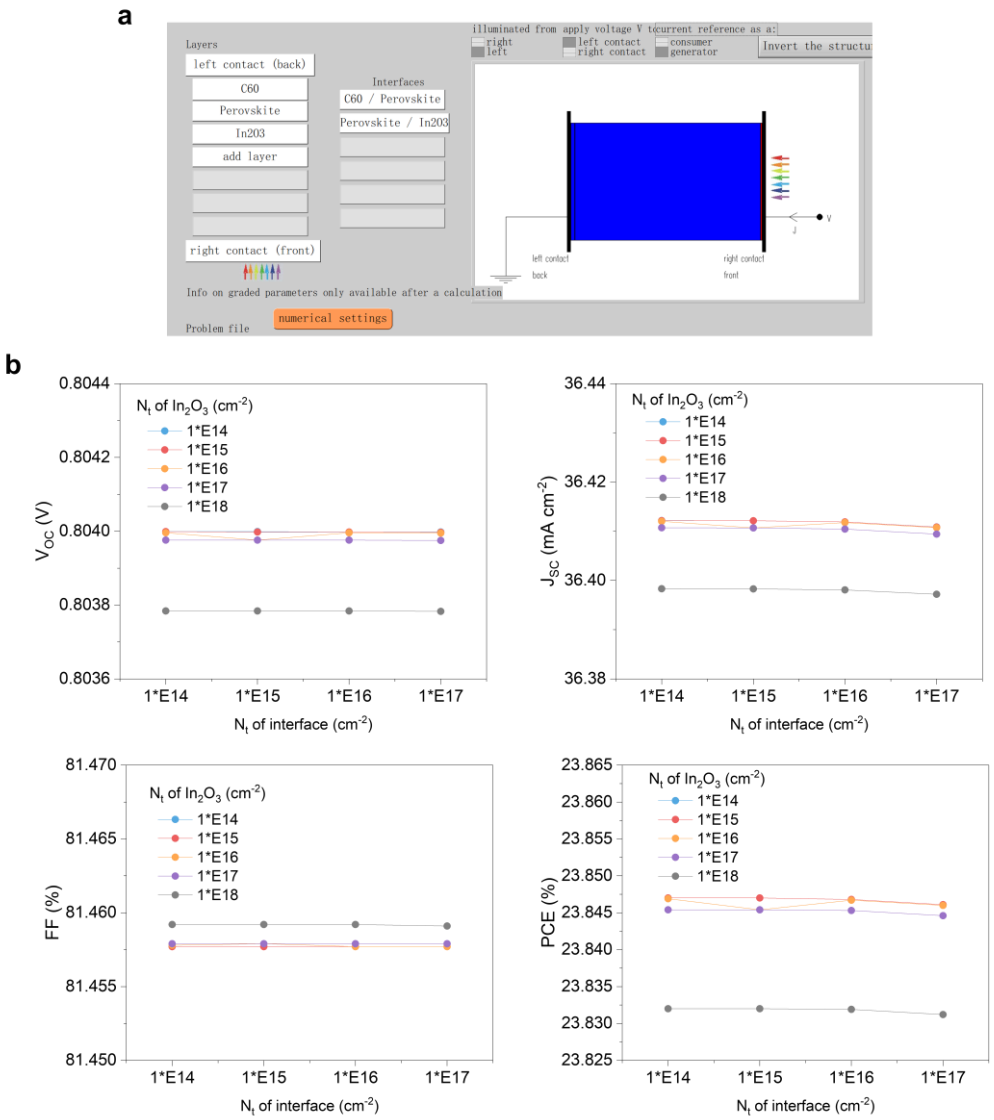

Supplementary Figure 19 | Electrical simulations using SCAPS-1D. (a) Electrical simulation of Pb-Sn perovskite solar cell configuration. (b) Simulated performance of the Pb-Sn perovskite solar cells with changed total trap density of In_2O_3 NC and the interface of In_2O_3/perovskite.

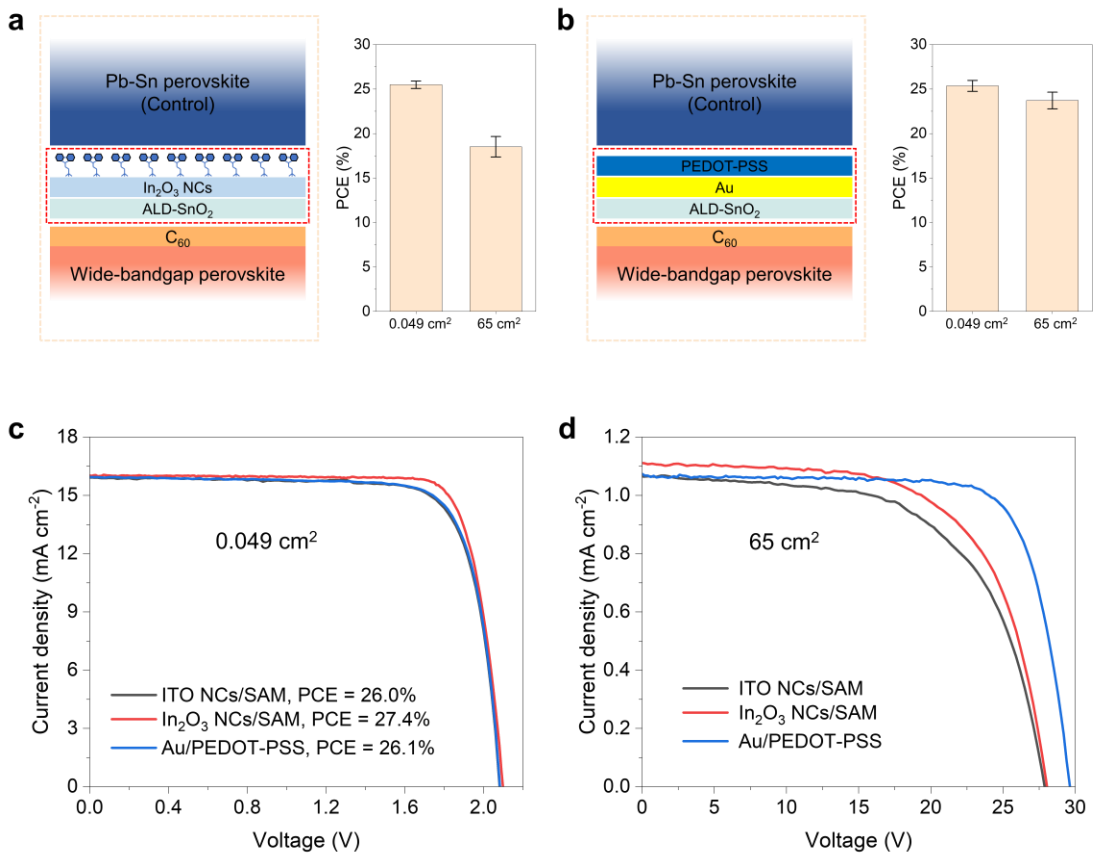

Supplementary Figure 20 | Performance and scalability of phosphonic acid-based carbazolyl derivatives in all-perovskite tandem solar cells and modules. (a and b) Schematic structure of the tandem device employing (a) SAM-modified In_2O_3 NCs and (b) conventional type-I structure. Each right panel shows the corresponding statistical performance distribution of small-area cells and large-area modules. 10 devices for each type. The error bar represents the standard deviation. (c) J-V curves of 0.049-cm^2 all-perovskite tandem solar cells using type-I structure and SAM-modified ITO or In_2O_3 NCs. (d) J-V curves of 65-cm^2 all-perovskite tandem modules using the same configurations. A significant loss in FF upon scaling is primarily caused by the limited scalability of the SAM, which restricts carrier transport.

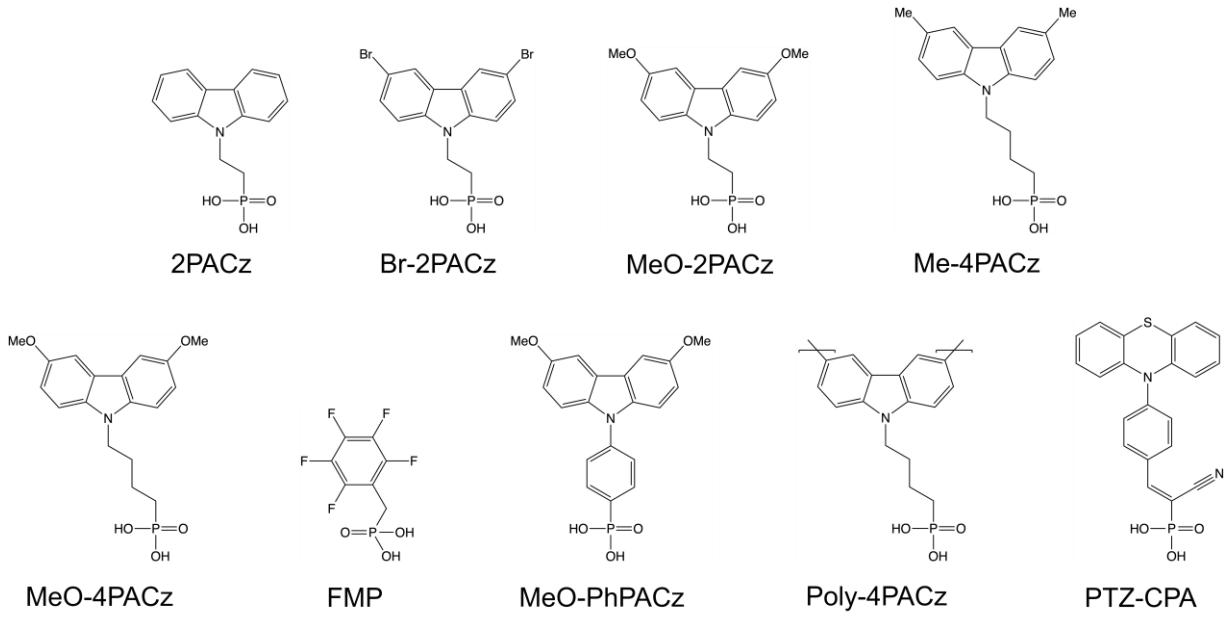

Supplementary Figure 21 | Molecular structural formulas of a library of hole-selective molecules. 2PACz: (2-(9H-carbazol-9-yl)ethyl)phosphonic acid; Br-2PACz: (2-(3,6-Dibromo-9H-carbazol-9-yl)ethyl)phosphonic acid; MeO-2PACz: (2-(3,6-Dimethoxy-9H-carbazol-9-yl)ethyl)phosphonic acid; Me-4PACz: [4-(3,6-Dimethyl-9H-carbazol-9-yl)butyl]phosphonic Acid; MeO-4PACz: [4-(3,6-Dimethoxy-9H-carbazol-9-yl)butyl]phosphonic Acid; FMP: ((perfluorophenyl)methyl)phosphonic acid; MeO-PhPACz: (4-(3,6-dimethoxy-9h-carbazol-9-yl)phenyl)phosphonic acid; Poly-4PACz: Poly(carbazole phosphonic acid); PTZ-CPA: (2-(4-(10H-phenothiazin-10- yl)phenyl)-1-cyanovinyl)phosphonic acid.

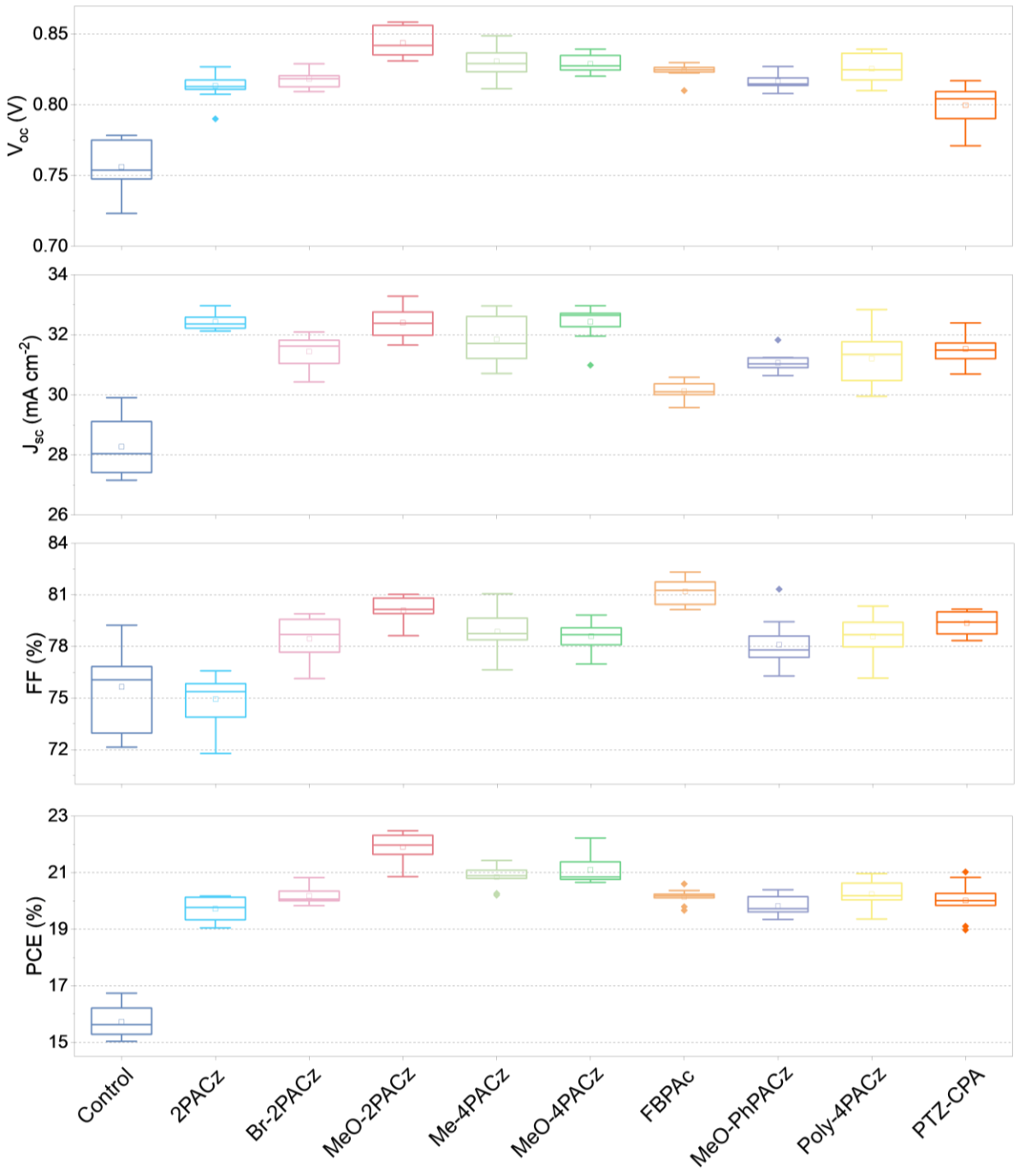

Supplementary Figure 22 | PCE comparison of PSCs using different HSMs. 12 devices with aperture area of 0.049 cm^2 were evaluated at each condition, and data are presented as mean ± standard deviation.

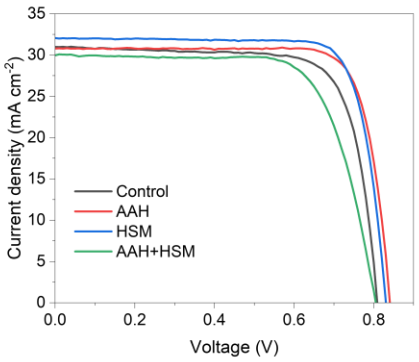

	V_{oc} (V)	J_{sc} (mA cm^{-2})	FF (%)	PCE (%)
Control	0.801	31.0	76.5	19.0
AAH	0.850	30.8	79.6	20.8
HSM	0.840	32.1	79.1	21.3
AAH/HSM	0.805	30.0	71.6	17.3

Supplementary Figure 23 | Photovoltaic performance of Pb-Sn perovskite solar cells with different additives.

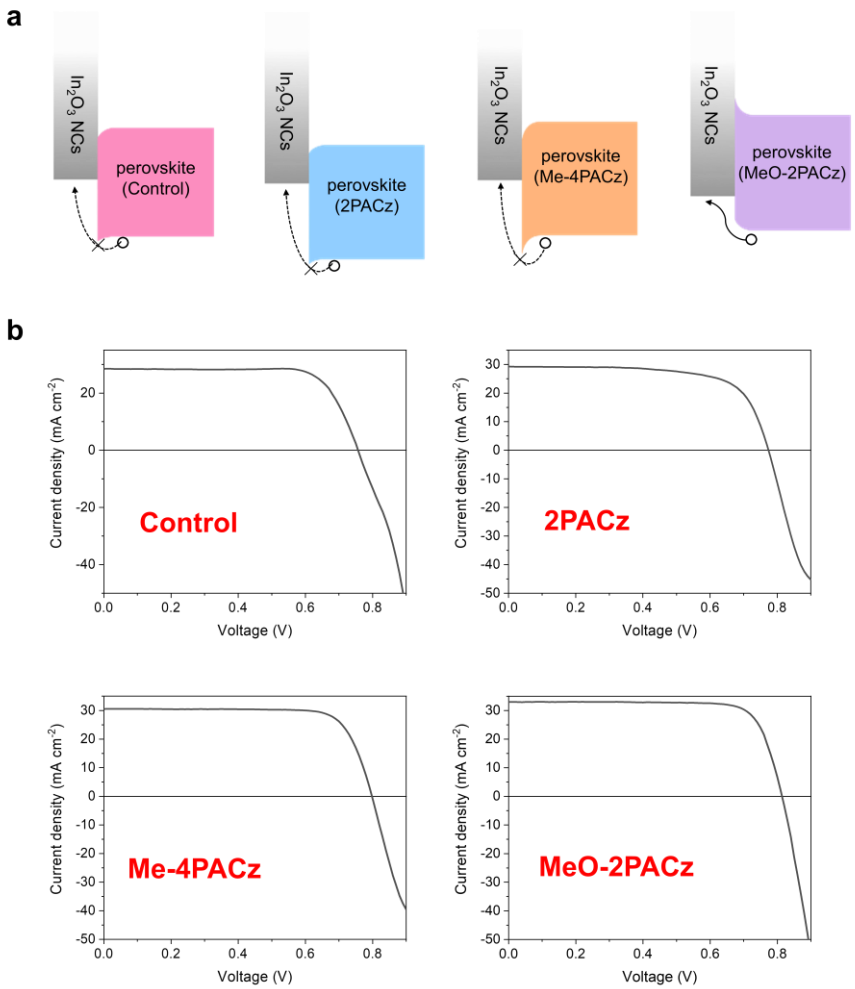

Supplementary Figure 24 | (a) Energy band alignment from UPS results between In_2O_3 NCs-MMPA and Pb-Sn perovskite with different HSMs. (b) J-V curves of the Pb-Sn perovskite solar cells with different HSMs.

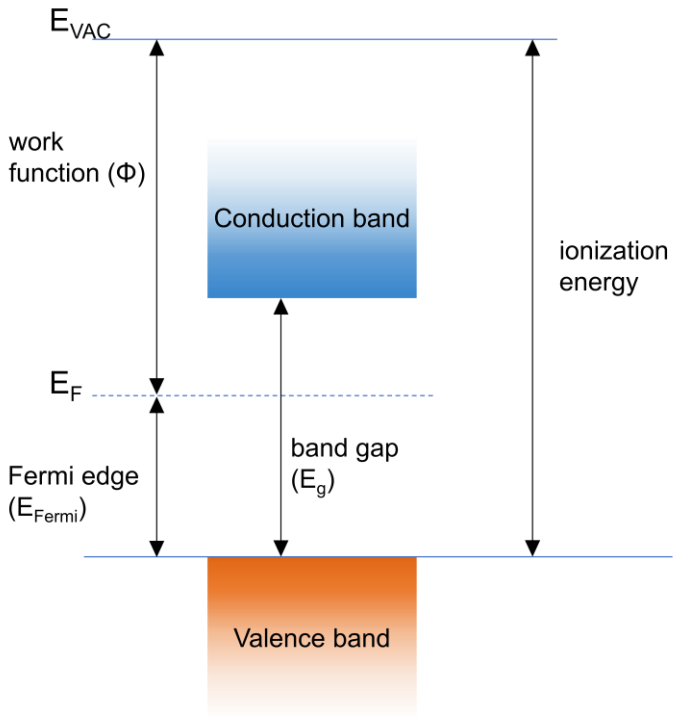

Supplementary Figure 25 | Schematic energy diagram of work function (Φ), Fermi edge (E_{Fermi}) and ionization energy (IE) on a semiconductor. We use $IE_{sam} = h\nu - \left|E_k^{cutoff} - E_k^{Fermi}\right|$ to determine the valence band maximum under bias voltage. The Fermi edge in bandgap can be determined without bias voltage.

Supplementary Note 2. Ligand selection and surface engineering of In_2O_3 nanocrystals

Surface ligands for In_2O_3 nanocrystals were designed through a stepwise ligand-engineering strategy to achieve stable surface anchoring, compatibility with industrial green-solvent processing, and tunable interfacial energy-level alignment while preserving nanocrystal size and crystal structure.

Oleylamine (OAm) was used as the initial ligand during nanocrystal synthesis. As a typical L-type amine ligand, OAm coordinates with precursor species and regulates nucleation and growth kinetics, enabling precise control over nanocrystal size, morphology, and crystallinity. However, the long hydrocarbon chain of OAm increases interparticle tunneling distances and limits charge transport[2], and OAm-capped nanocrystals are typically dispersible only in nonpolar solvents such as toluene, which are incompatible with industrial green-solvent processing[1].

To enable green-solvent processing, mono-2-(methacryloyloxy)ethyl succinate (MMES) was introduced via ligand exchange. MMES contains a carboxylic acid anchoring group capable of coordinating with surface In^{3+} sites and polar functional groups compatible with the industrial solvent propylene glycol monomethyl ether acetate (PGMEA)[3,4]. Replacement of OAm by MMES forms stable carboxylate–In coordination and enables stable nanocrystal dispersion in PGMEA without altering nanocrystal size or crystallinity. The surface binding of MMES was confirmed by broadened ^1H NMR signals after ligand exchange, while TEM and XRD measurements verify that the nanocrystal morphology and lattice structure remain unchanged.

To further tune the electronic structure, the ligand MMPA was designed by introducing a conjugated phenyl unit into the MMES framework. This modification increases molecular rigidity and modifies the molecular dipole, thereby modulating the interfacial electrostatic environment. Ultraviolet photoelectron spectroscopy (UPS) shows that ligand modification systematically shifts the Fermi level of In_2O_3 nanocrystals from −3.62 eV (OAm) to −4.49 eV (MMES) and −4.86 eV (MMPA), demonstrating that ligand-induced dipole engineering enables precise tuning of the nanocrystal work function and interfacial energy-level alignment.

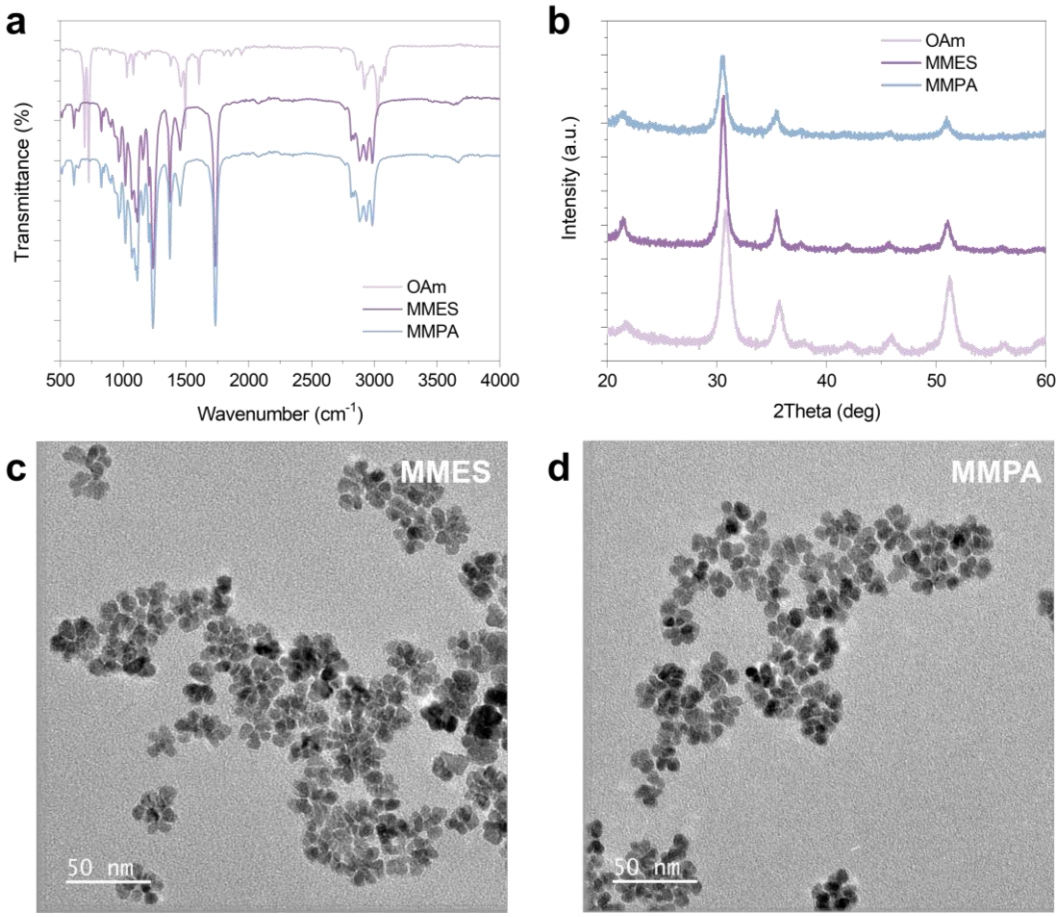

Supplementary Figure 26 | Characteristics of In_2O_3 NCs with different ligands. (a) FTIR spectra and (b) XRD patterns of In_2O_3 NCs with different ligands. TEM images of (c) MMES- and (d) MMPA-capped In_2O_3 NCs. The morphology of the In_2O_3 NCs remained unchanged following the ligand exchange.

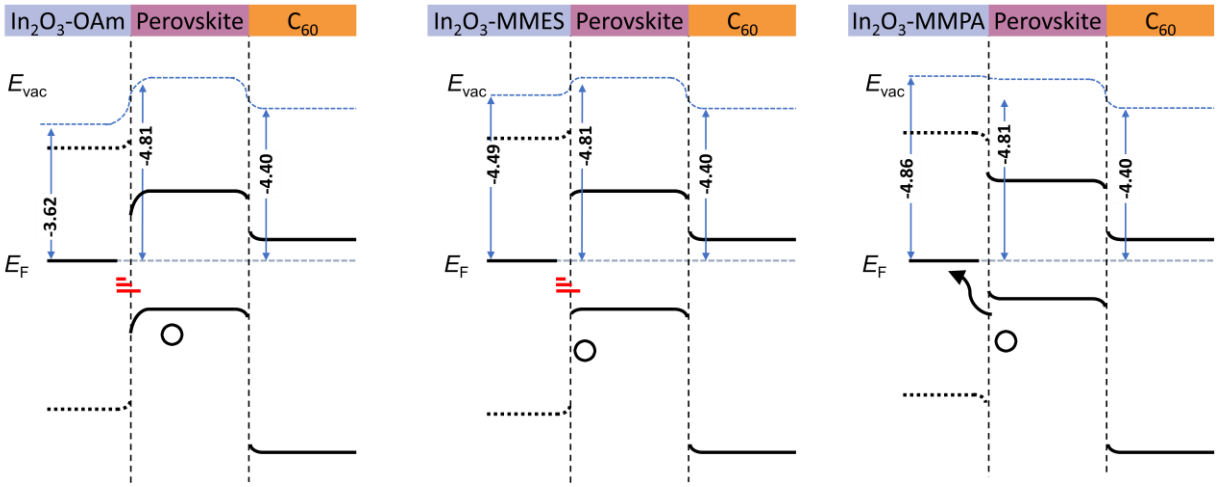

Supplementary Figure 27 | Energy band diagrams at the interface of the target perovskite film and In_2O_3 NCs with different ligands. The perovskite shows energy barriers while contact with OAm- and MMES-capped In_2O_3 NCs, hindering the hole transport at the interface.

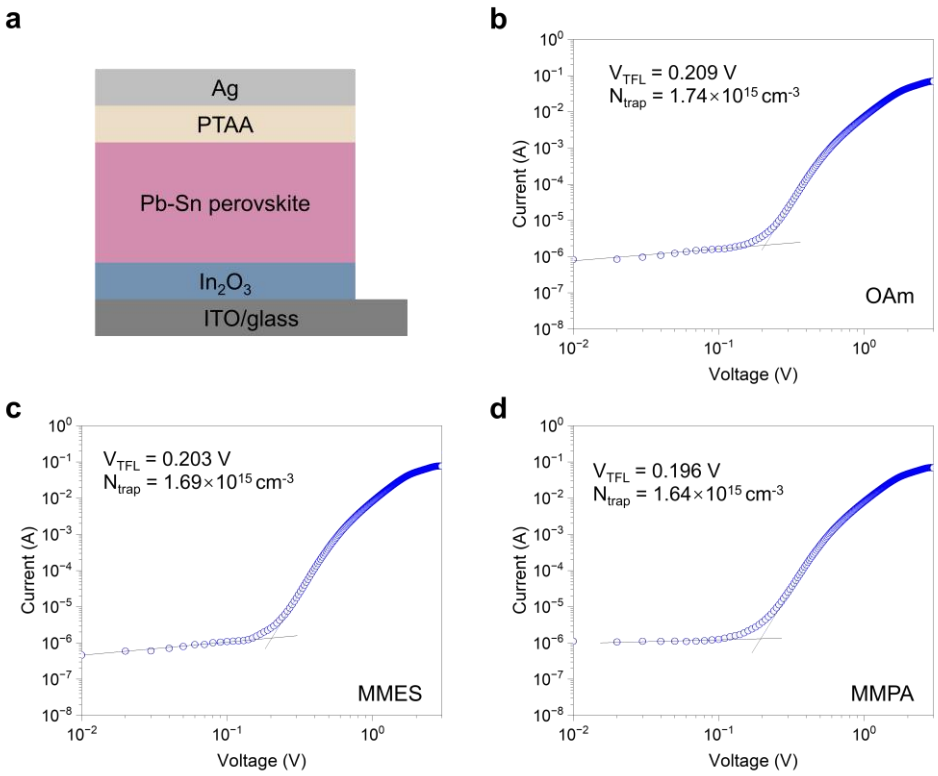

Supplementary Figure 28 | Current-voltage traces and trap density of Pb-Sn perovskites as determined by the SCLC method. (a) Hole-only device structure constructed to obtain the hole trap density. The trap density N_{trap} is determined by the equation: $V_{TFL}=qN_{trap}L^2/(2\varepsilon\varepsilon_0)$, where V_{TFL} is trap-filled limit voltage, L is the thickness of perovskite film, ε is the relative dielectric constant of perovskite, and ε_0 is the vacuum permittivity. (b-d) I-V curves of the hole-only devices using In_2O_3 NCs with (b) OAm, (c) MMES and (d) MMPA.

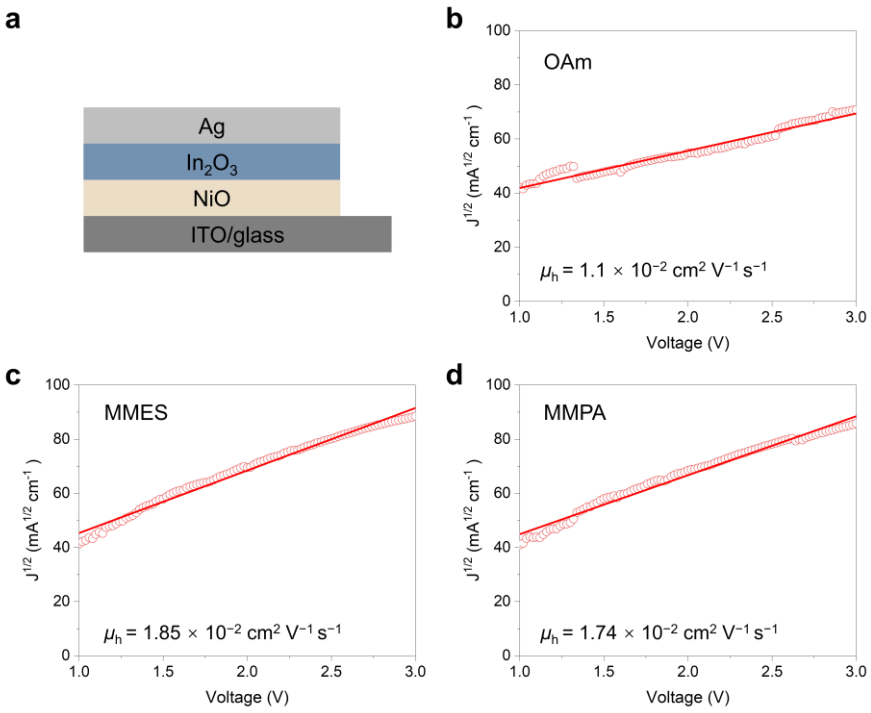

Supplementary Figure 29 | Measurement of hole mobility by the SCLC model. (a) Device structure constructed to obtain the hole mobility. The hole mobility μ_h is determined by the Mott-Gurney law: $\mu_h=8JL^3/(9\varepsilon_0\varepsilon_r V^2)$, where J is the current density, L is the thickness of In_2O_3 NCs, ε_0 is the vacuum permittivity, and ε_r is the dielectric permittivity of In_2O_3 NCs. (b-d) $J^{1/2}$-V curves of the hole-only devices using In_2O_3 NCs with (b) OAm, (c) MMES and (d) MMPA.

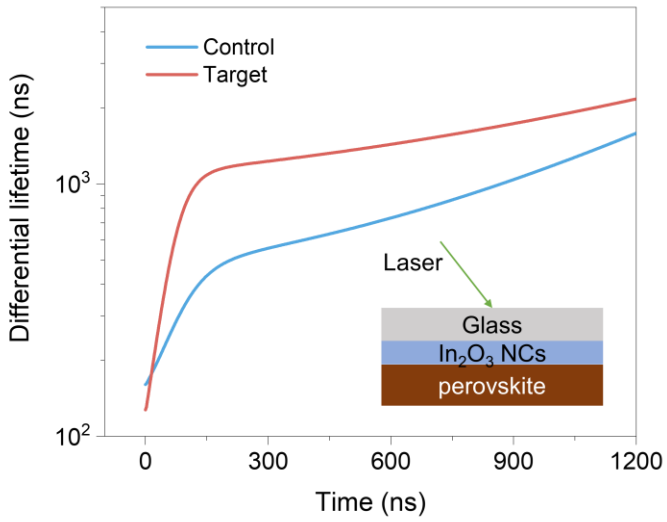

Supplementary Figure 30 | Differential lifetime of control and target perovskite films deposited on MMPA-In_2O_3 NCs/glass substrates.

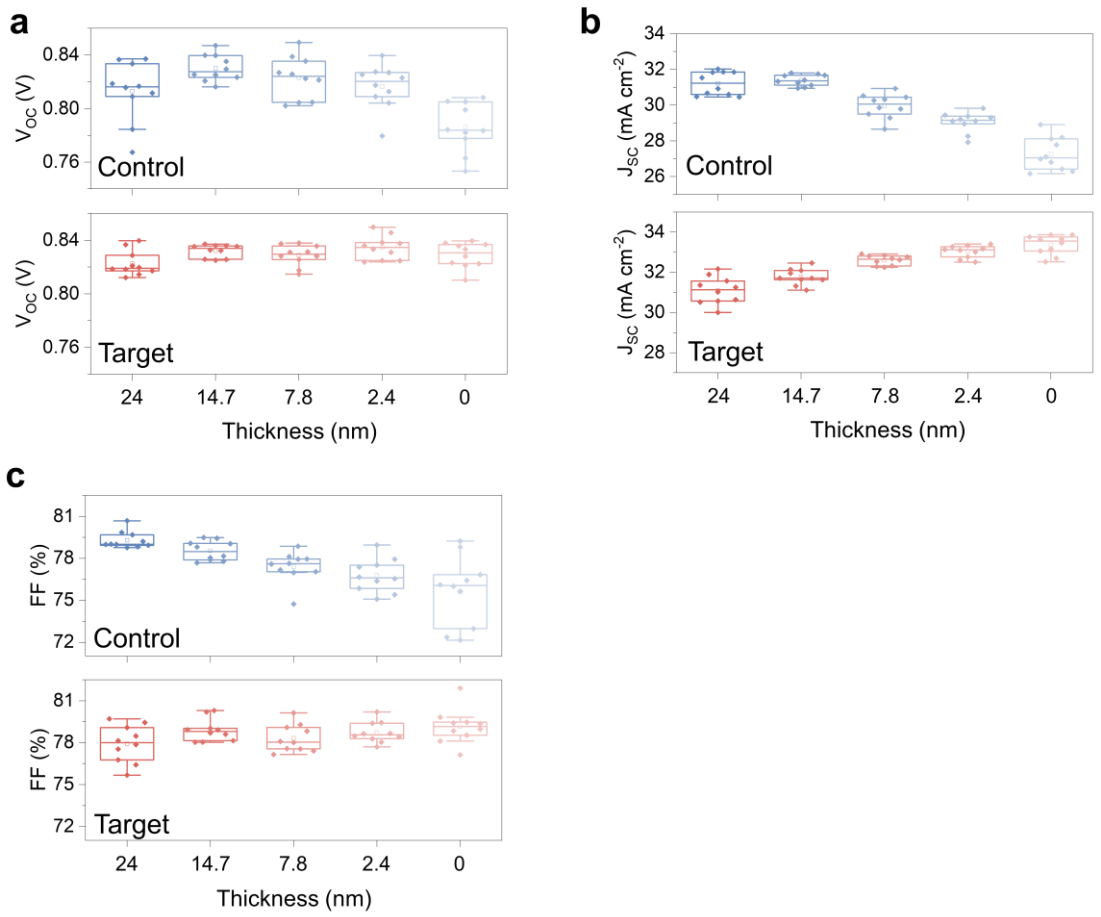

Supplementary Figure 31 | Photovoltaic performance statistics of control and target Pb-Sn PSCs with reduced PEDOT-PSS thickness. (a) V_{OC}. (b) J_{SC}. (c) FF. The statistical PCE is shown in Fig. 2e. 10 devices for each type with aperture area of 0.049 cm^2. The boxes and whiskers represent the standard deviation and the maximum and minimum of the distributions, respectively.

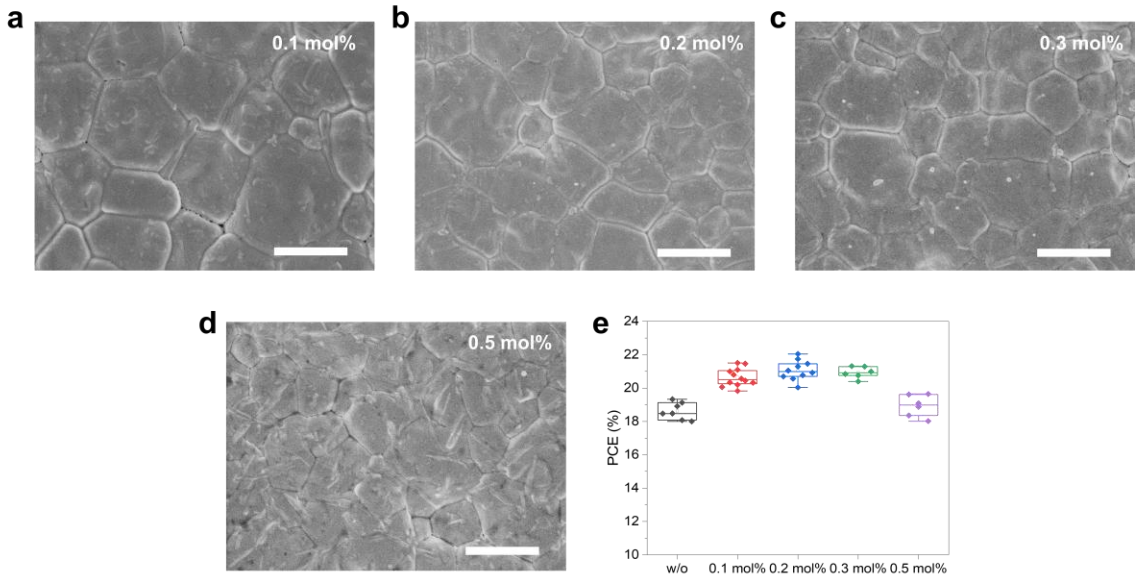

Supplementary Figure 32 | Film morphology and device performance with different concentration of the incorporated HSM. SEM images of the perovskite films with different concentration of the incorporated HSM, (**a**) 0.1 mol%; (**b**) 0.2 mol%; (**c**) 0.3 mol%; (**d**) 0.5 mol%; (**e**) PCE statistics of the Pb-Sn PSCs, with different concentration of HSMs. The optimal condition is 0.2% mole ratio. The box plots show the PCE distributions for devices fabricated with 7, 12, 10, 6, and 6 individual cells at each concentration, respectively. All devices have an aperture area of 0.049 cm^2. The boxes represent the standard deviation, and the whiskers indicate the maximum and minimum values of each distribution.

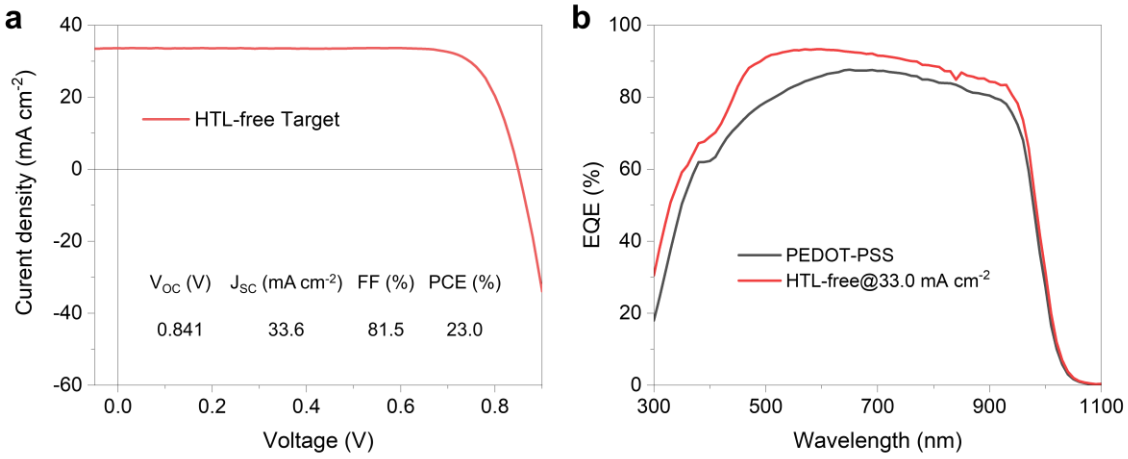

Supplementary Figure 33 | Performance of the champion HTL-free device. (A) J-V curve of the HTL-free device using target perovskite film. (B) Corresponding EQE spectra of the HTL-free and PEDOT-PSS-based devices.

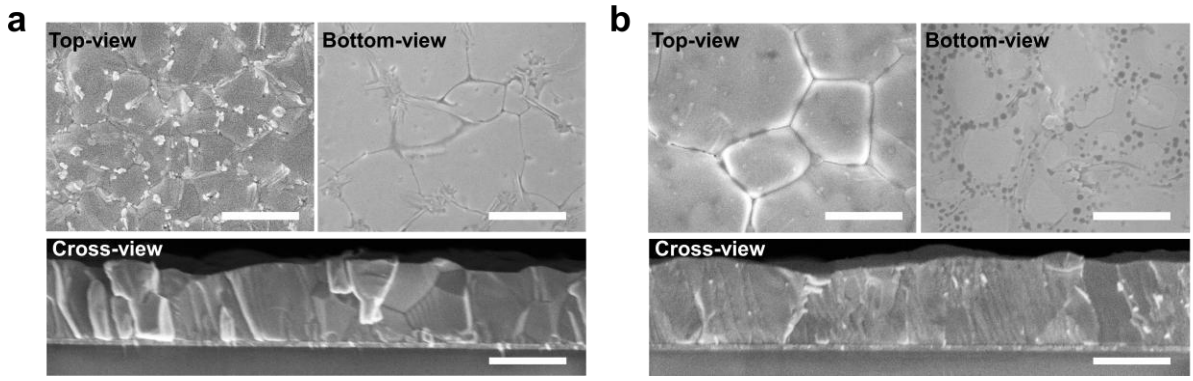

Supplementary Figure 34 | Surface morphology of HSM incorporated Pb-Sn perovskites. Top-, bottom-, and cross-view SEM images of control (a) and target (b) perovskite films. All the scale bars are 1 μm.

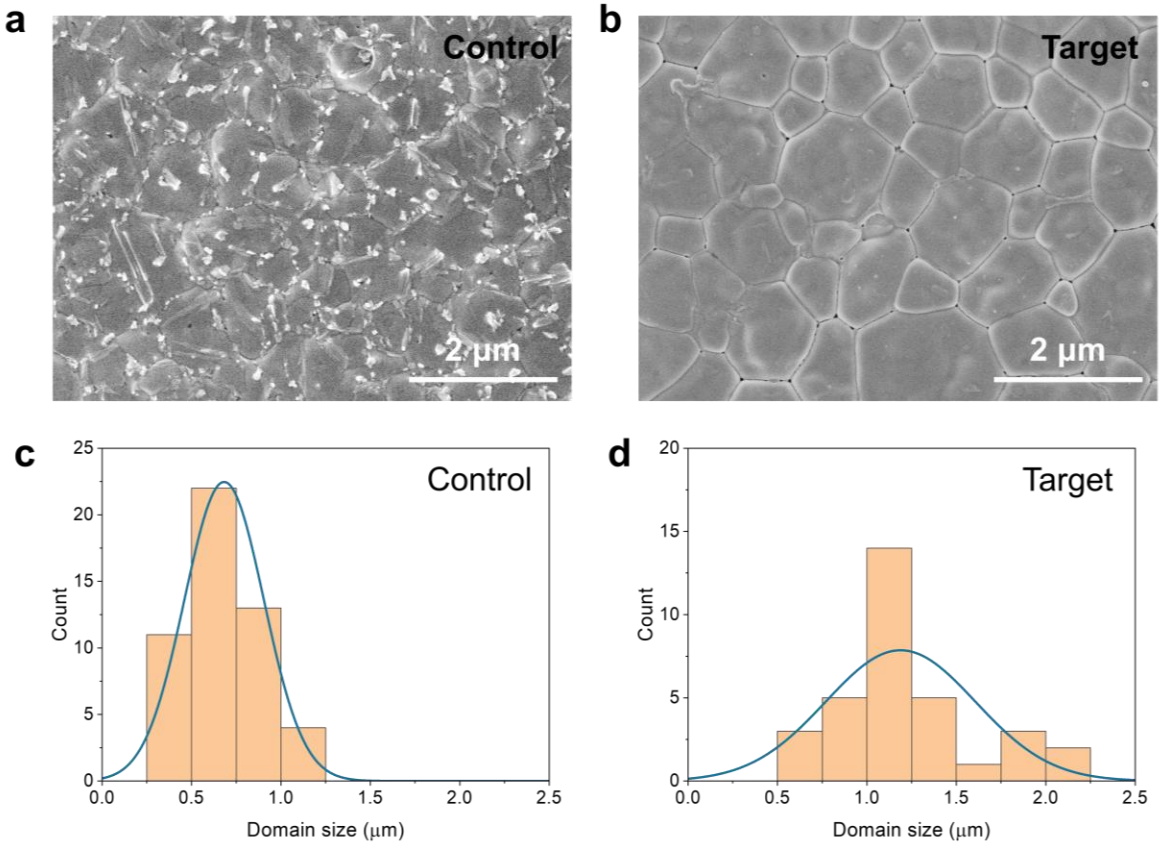

Supplementary Figure 35 | Film morphology of control (a) and target (b) Pb-Sn perovskite films and crystal domain statistics of corresponding control (c) and target (d) film. The target perovskite film shows clean film surface with larger domains compared with control film.

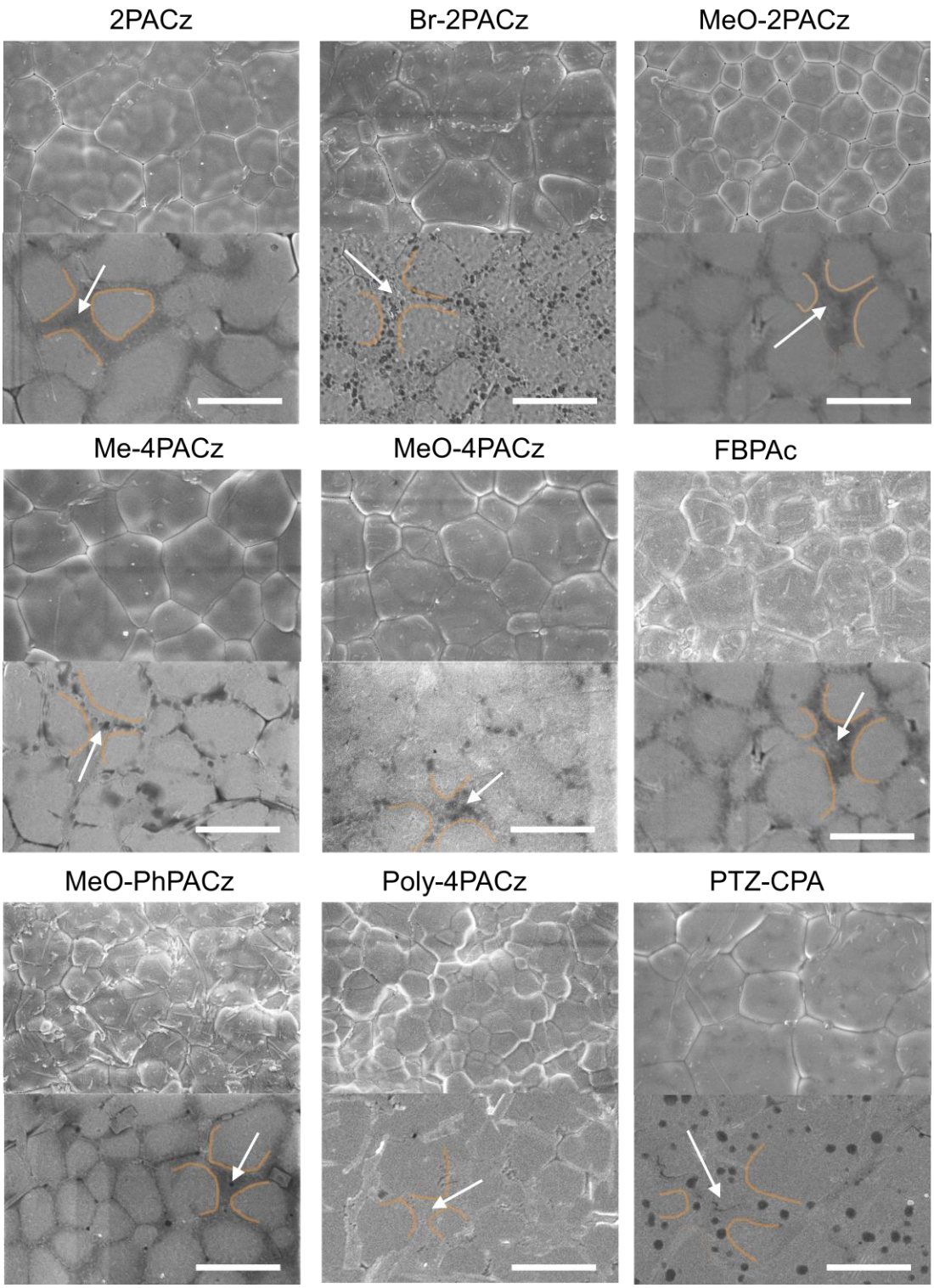

Supplementary Figure 36 | Top- and bottom-view of perovskite films with different HSMs. The area indicated by the arrow is the boundaries with enriched HSMs.

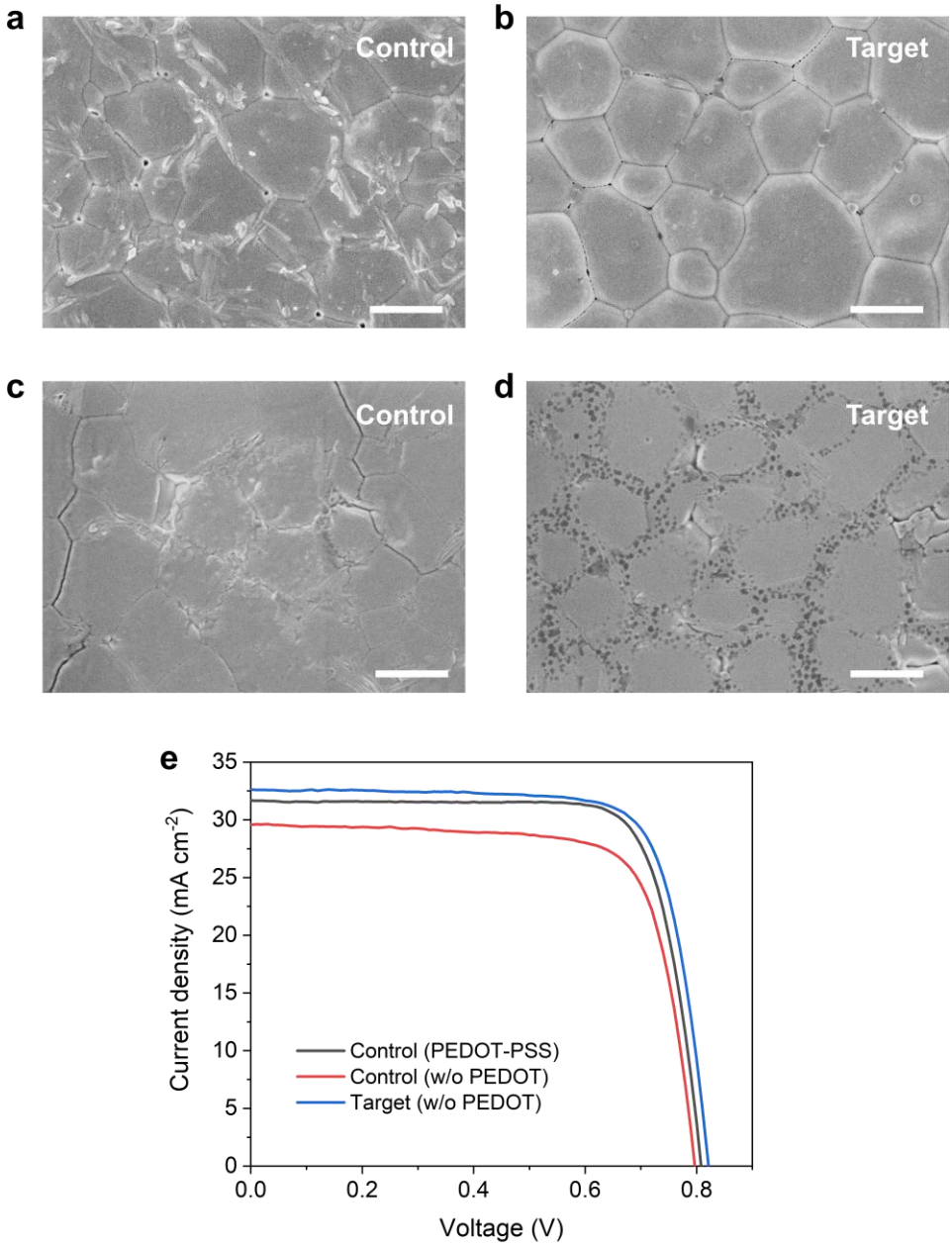

Supplementary Figure 37 | The surface morphology and performance of Pb-Sn perovskite fabricated using DMF-based solvent system. (a-b) Top- and (c-d) bottom-view SEM images of control and target perovskite films. (e) J-V curves of Pb-Sn perovskite solar cells.

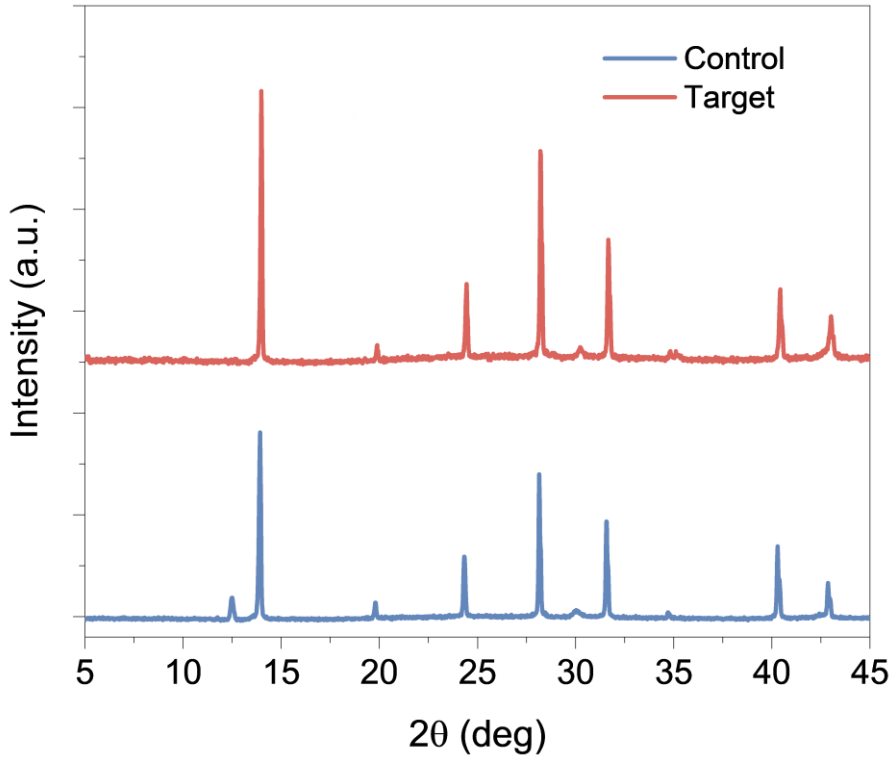

Supplementary Figure 38 | XRD patterns of the control and target Pb-Sn perovskite films.

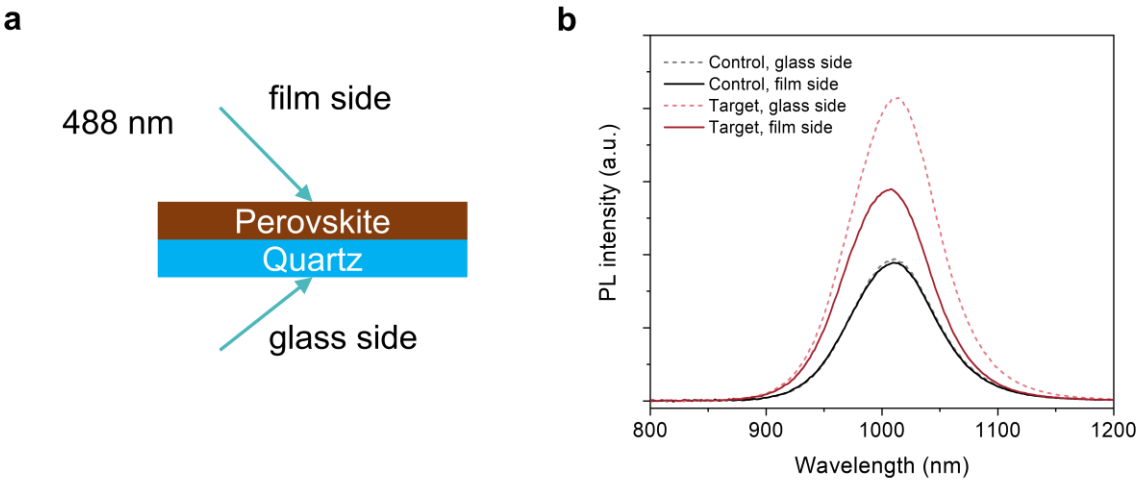

Supplementary Figure 39 | PL spectra measured from top and bottom surface. (a) The excitation from both the top of perovskite film and the bottom of glass sides; (b) Steady-state PL spectra of control and target perovskite films deposited on bare glass. The PL of the control perovskite film shows identically strong, while the PL from the glass side of the target film is higher than that from film side. It indicates that the buried anchored HSM reduces the interface defects.

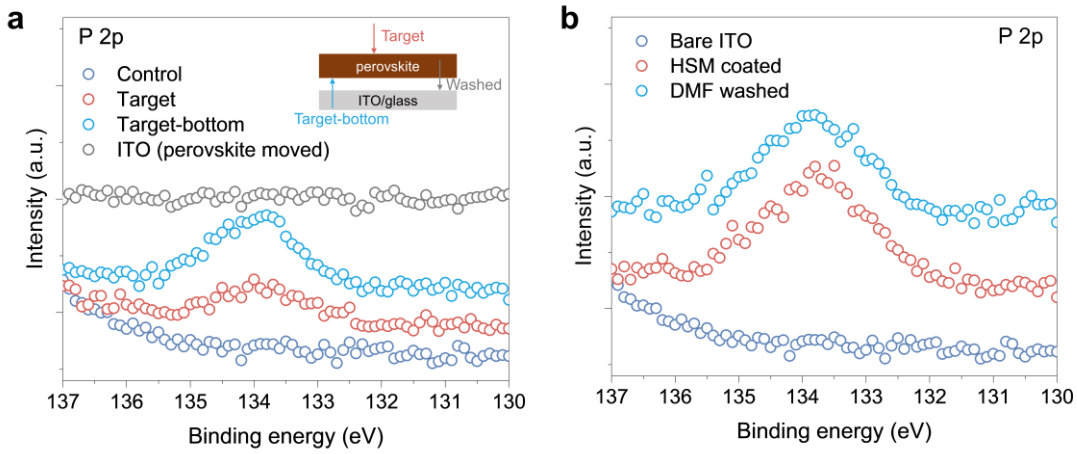

Supplementary Figure 40 | The P 2p XPS spectra of different film surfaces. (a) Insert is a schematic of the location of the XPS probe. It revealed that the distribution of HSM at the bottom interface of the perovskite film was higher than that at the top surface, while no HSM residue was found on the ITO surface after washing with DMF. (b) After DMF washing, the anchored self-assembled molecular still existed on the ITO substrates. The phosphorus signal persists after washing, confirming that the phosphonic acid anchoring group can form a stable bond with the ITO surface when directly deposited. These results collectively demonstrate that in our solution-processed architecture, HSM preferentially interacts with perovskite components during crystallization rather than forming a SAM on ITO, explaining its removal together with the perovskite phase upon solvent washing.

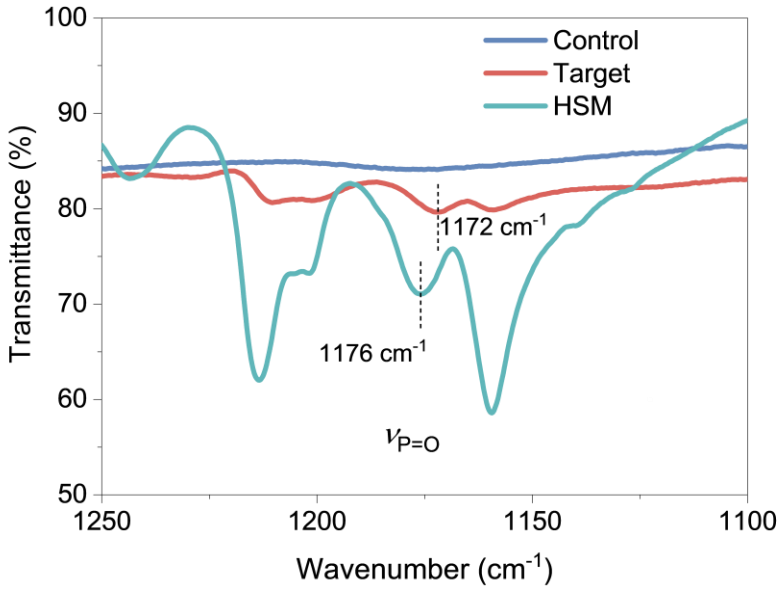

Supplementary Figure 41 | FTIR spectra of HSM powder and control, target perovskite powders scraped from ITO substrates.

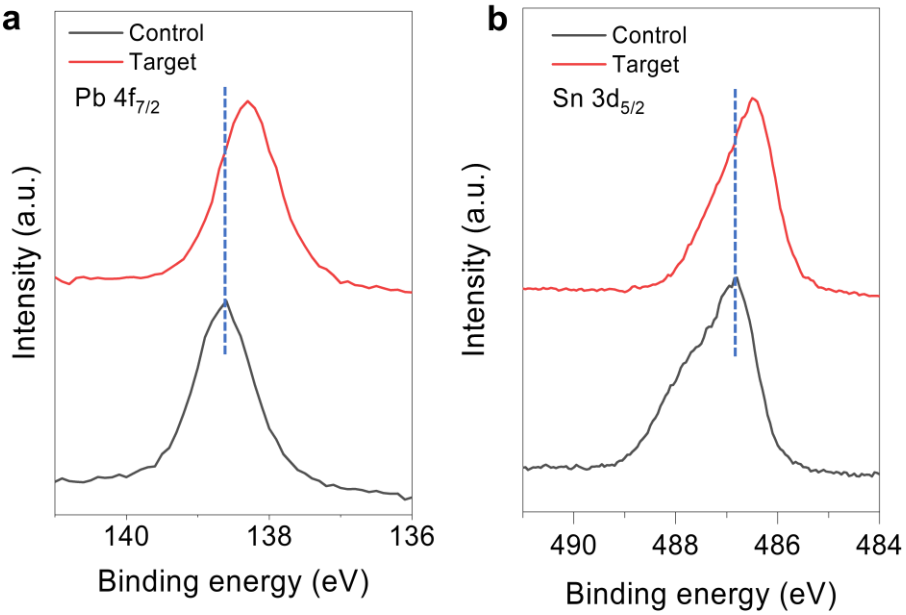

Supplementary Figure 42 | XPS spectra of the control and target Pb-Sn perovskite films. (a) Pb 4f7/2 and (b) Sn 3d5/2. The decreased binding energies of Pb 4f7/2 and Sn 3d5/2 indicated the formation of HSM-Pb/Sn adducts.

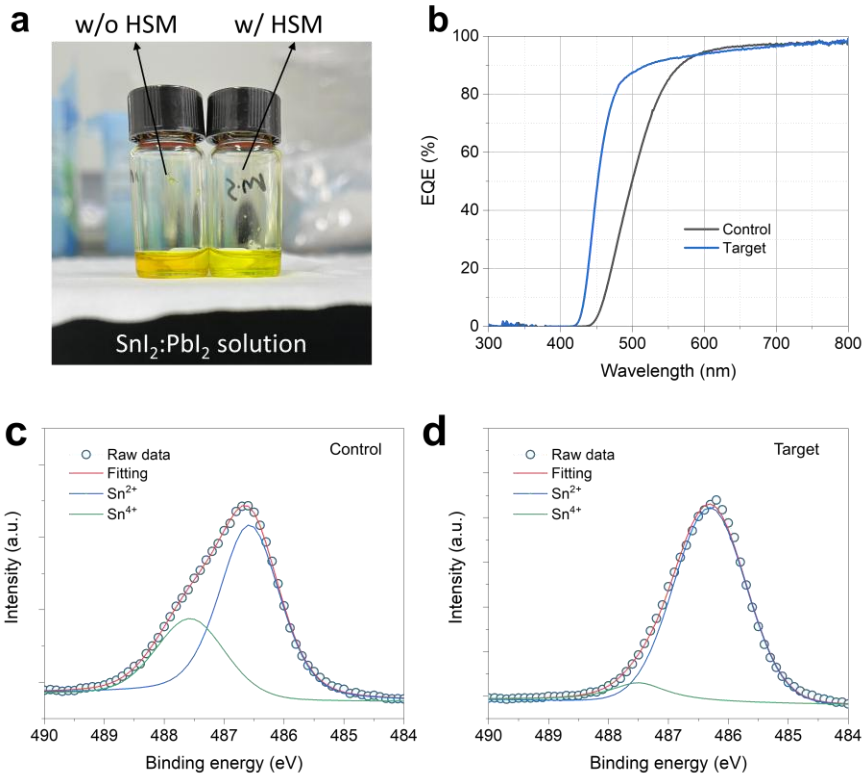

Supplementary Figure 43 | Oxidation suppression with HSM incorporation. (a) Digital photo of the SnI_2:PbI_2 mixed solution with and without HSM; (b) Corresponding optical absorption of the solution with and without HSM; (c and d) XPS spectra of Sn 3d for (c) control and (d) target Pb-Sn perovskite films.

Supplementary Note 3. The optical-pump terahertz-probe (OPTP) measurements.

As a contact-free spectroscopic methodology, the optical-pump terahertz-probe (OPTP) system has emerged as a powerful experimental platform for characterizing transient charge transport phenomena in thin-film semiconductor architectures[5–9]. This all-optical configuration circumvents measurement artifacts inherent to electrode-based characterization of mesoporous systems. The non-destructive nature of terahertz (THz) radiation interrogation (photon energy ~4.1 meV at 1 THz) permits precise quantification of photoexcited carrier density and transport characteristics via conductivity modulation analysis. Crucially, THz spectroscopic responses remain selectively decoupled from excitonic polarization and trap-state interference, enabling direct extraction of complex conductivity tensor components without reliance on Kramers-Kronig reconstruction protocols.

Supplementary Fig. 44 presents comparative analyses of time-resolved THz transmission modulations in control and target thin-film specimens (thickness: ~1100 nm) across multiple excitation densities. Photocarrier generation was achieved using 1.55 eV laser excitation (spot diameter: ~5 mm), with subsequent conductivity evolution monitored through phase-stable sub-picosecond THz probe pulses. Spectral decomposition of both amplitude and phase parameters was accomplished via electro-optic detection with temporal resolution below 100 fs.

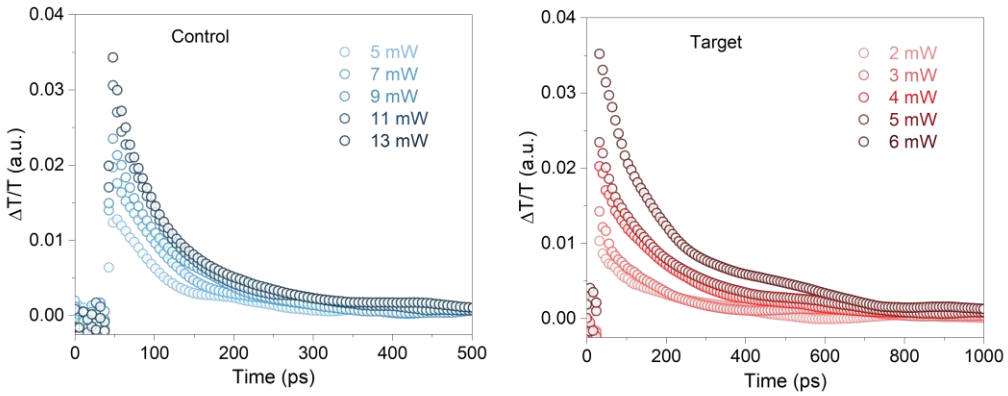

Supplementary Figure 44 | Free carrier dynamics of the control and target samples based on OPTP method.

The frequency-dependent photoconductive response of the thin-film systems was determined through simultaneous analysis of THz waveform amplitude attenuation and phase-shift perturbations. Charge transport parameters were quantified using a modified Drude-Smith

formalism accounting for carrier scattering dynamics and momentum relaxation effects. Notably, in perovskite architectures with subwavelength dimensions (~600 nm thickness,), the surface-confined conductivity tensor can be mathematically represented as[8]:

$$\Delta\sigma_{sheet} = \frac{n_A + n_B}{Z_0} \cdot \frac{\Delta T(\omega, \Delta t)}{T(\omega)} \qquad (1)$$

Equation (1) defines the normalized THz field variation, where $T(\omega)$ and $T_{excited}(\omega, \Delta t)$ correspond to unperturbed and photoinduced transmission states, respectively. Considering the minimal thickness contrast between the perovskite layer and quartz substrate, the analytical framework incorporates optical constants of ambient atmosphere ($n_A = 1$) and crystalline quartz ($n_B = n_{quartz} = 1.95$). The derived conductivity values maintain strict proportionality with the observed THz field variations through this analytical framework.

To explicitly address momentum relaxation anomalies in structurally disordered materials, the Drude-Smith theoretical framework introduces a first-order correction term to the complex conductivity tensor[8]:

$$\Delta\sigma_{Drude-Smith}(\omega) = \frac{\varepsilon_0 \omega_p^2 \tau}{1 - i\omega\tau}\left(1 + \frac{c_1}{1 - i\omega\tau}\right) \qquad (2)$$

Three parameters were obtained from experimental data fitting: Drude plasma frequency ω_p, backscattering constant c_1 (ranging from -1 to 0), and momentum relaxation time τ. Free carrier density N and mobility μ were calculated using[8]:

$$N = \varepsilon_0 \omega_p^2 m^* / e^2 \qquad (3)$$

$$\mu = e\tau(1 + c_1) / m^* \qquad (4)$$

Where $m^* = 0.2 m_e$ denote the effective mass, ε_0 the vacuum permittivity, and τ the average time interval.

Quantitative analysis employing the Drude-Smith formalism on the THz photoconductivity datasets (**Supplementary Fig. 45**) revealed systematically enhanced charge transport metrics, with extracted carrier mobility values of 20 and 36 $cm^2\ V^{-1}\ s^{-1}$, respectively.

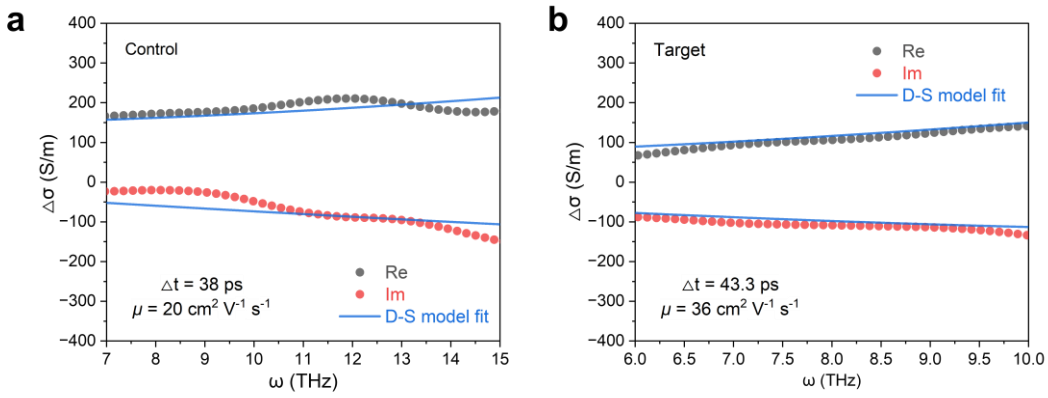

Supplementary Figure 45 | Frequency-dependent complex photo-induced conductivity of (a) control and (b) target samples. The blue solid lines indicated the fitted Drude-Smith model.

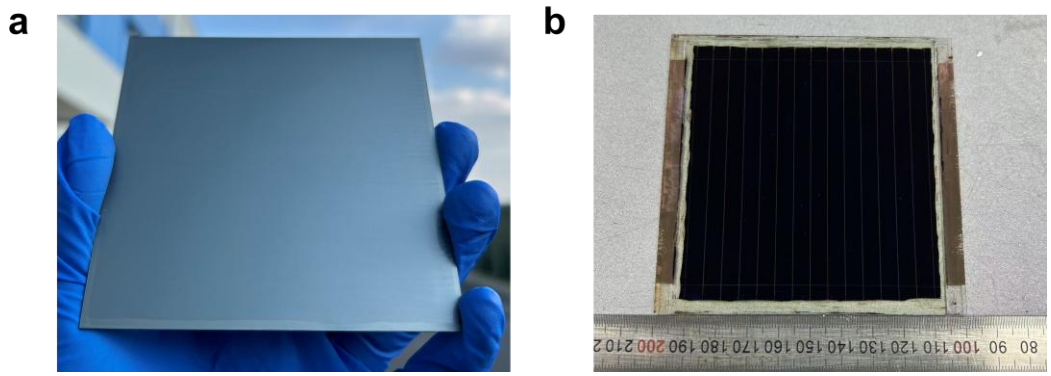

Supplementary Figure 46 | Digital photos of (a) the Pb-Sn perovskite film and (b) a single-junction solar module deposited on 10×10 cm^2 substrates.

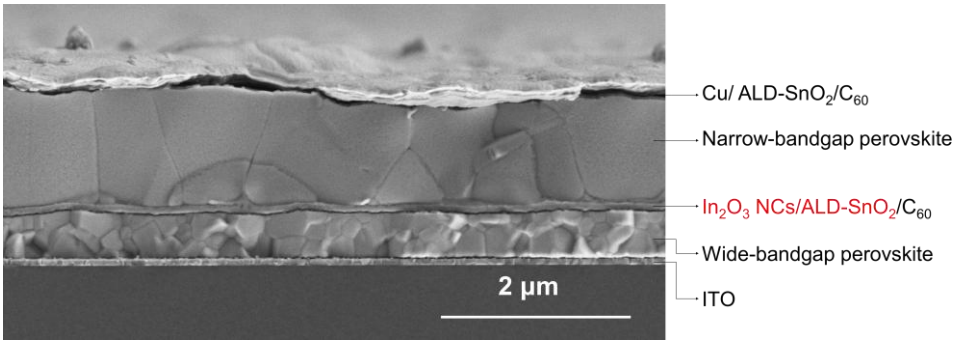

Supplementary Figure 47 | Cross-sectional SEM of the all-perovskite tandem structure from a TSM.

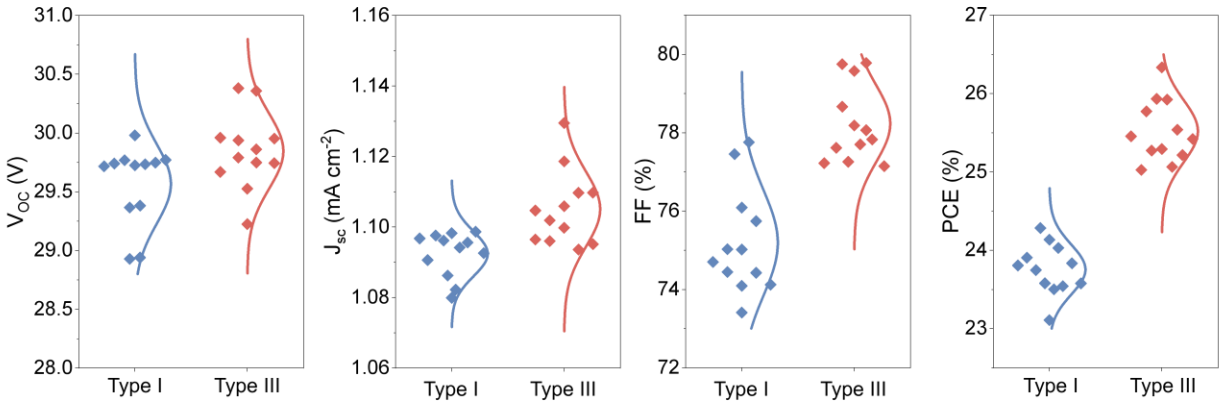

Supplementary Figure 48 | Photovoltaic parameter statistics of 65-cm^2 all-perovskite TSMs. 12 devices for each type. The distribution curve represents the Gaussian fitting.

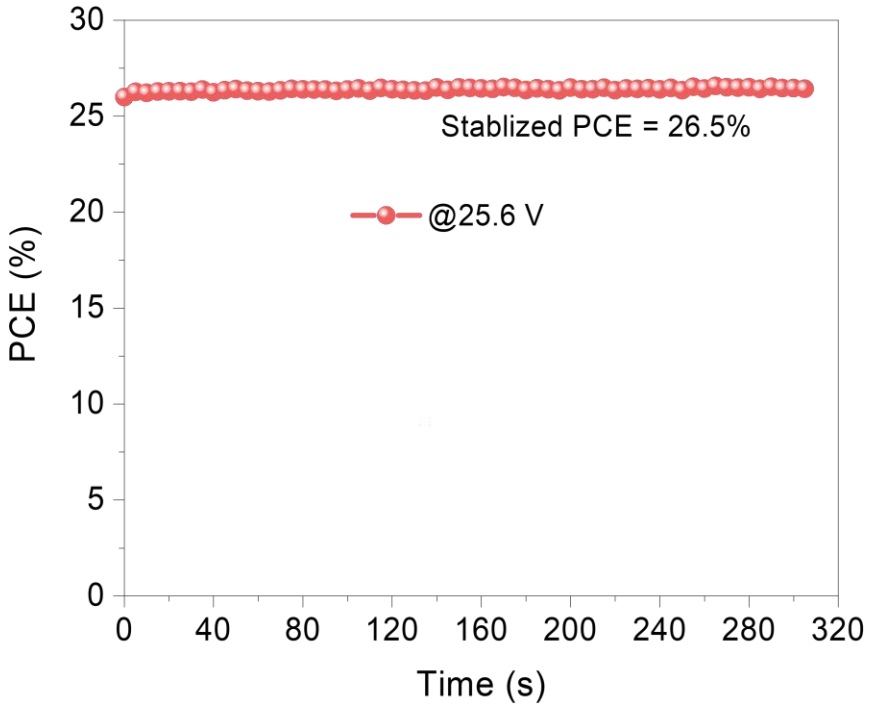

Supplementary Figure 49 | Steady-state output of the champion TSM.

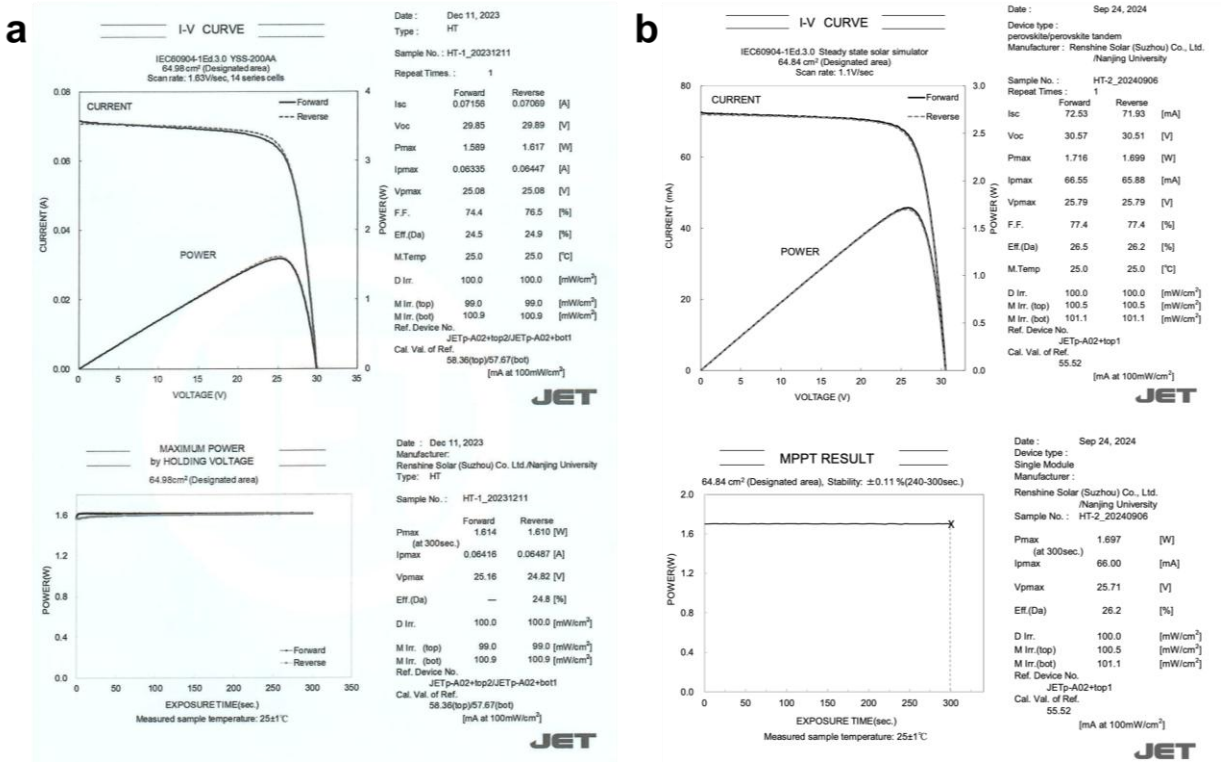

Supplementary Figure 50 | The certificated results of (a) Type-I and (b) Type-III all-perovskite TSMs with aperture area of ~65 cm^2 measured by Japan Electrical Safety and Environment Technology Laboratories.

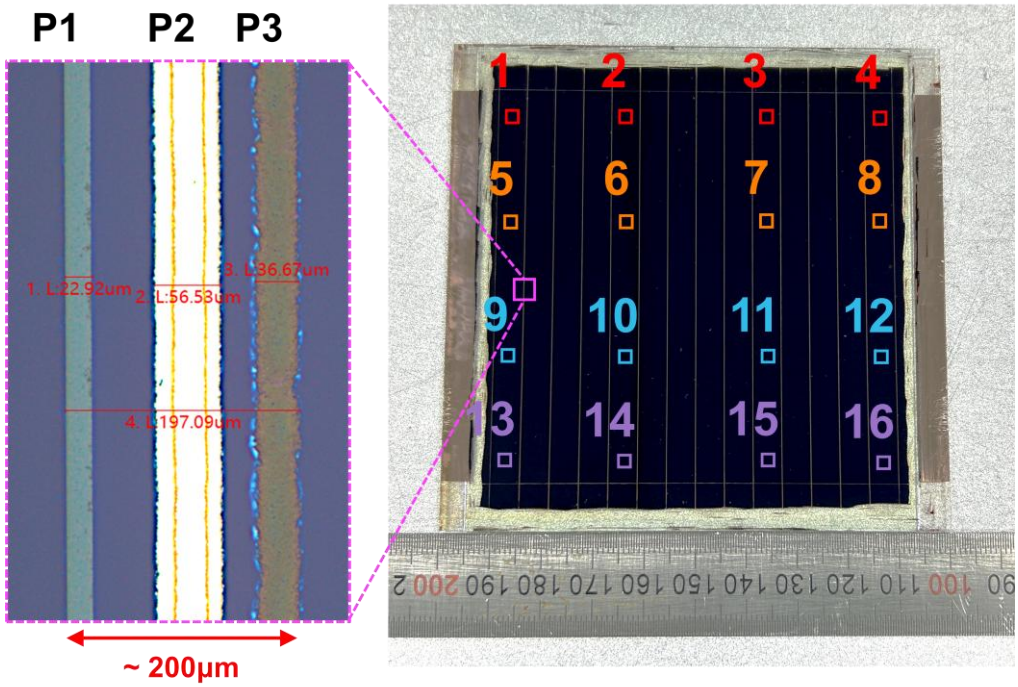

Supplementary Figure 51 | Photos of the laser-scribing all-perovskite TSM deposited on 10×10 cm^2 substrate with an aperture area of 65 cm^2. The left optical microscope shows that the death width (from P1 left to P3 right) is about ~200 μm, achieving a high geometric fill factor of 96.5%. The EQE uniformity is measured from the selected 16 points in the right digital photo.

Supplementary Note 4. Optimization of laser scribing parameters for module fabrication.

This note provides supplementary details on the optimization of the laser scribing processes (P1, P2, P3) used to fabricate the high-performance modules discussed in the main text. The optimization focused on three key aspects: wavelength selection, dead zone width, and P2 scribing energy.

1. Laser wavelength selection

To achieve clean and reliable pattern definition, three different laser wavelengths were evaluated for the P1, P2, and P3 scribing steps: infrared (1064 nm), green (532 nm), and ultraviolet (355 nm). The selection was based on the resulting scribe morphology, process stability, and material compatibility.

Based on these criteria, the optimal configuration was determined to be a 1064 nm laser for the P1 step and a 532 nm laser for both the P2 and P3 steps. It is noteworthy that the 355 nm laser produced ablation quality comparable to the 532 nm source, as illustrated in **Supplementary Fig. 52**. However, the 532 nm laser was ultimately adopted for the P2 and P3 processes due to its superior operational stability and higher throughput in our experimental setup.

2. Optimization of interconnection dead area width

The total interconnection dead area was optimized to balance aperture efficiency against manufacturing yield. This was achieved by systematically shifting the P2 and P3 scribes closer to the P1 scribe, as depicted in **Supplementary Fig. 53**.

By adjusting the scribe positions, the dead zone width was successfully reduced from an initial value of 200 μm down to 160 μm and 155 μm. However, electrical characterization revealed that this reduction did not result in a significant improvement in the module's current density. Furthermore, reducing the dead zone to 155 μm increased the risk of electrical shunting due to undesirable contact or intersection between the P1 and P2 scribes, leading to a noticeable decrease in production yield. Consequently, a dead zone width of 160 μm was selected as the optimal compromise, ensuring both high aperture efficiency and robust process reliability.

3. Optimization of P2 scribing pulse energy

The P2 process, which requires the precise removal of the absorber layer to expose the underlying transparent conductive oxide (TCO) without damaging it, was identified as the most critical step for series interconnection. To determine the optimal processing window, the laser pulse energy for the P2 scribe was varied systematically.

As shown in **Supplementary Fig. 54**, the pulse energy was increased from a regime of insufficient ablation (where residual absorber material remained, hindering conductivity) to a regime of excessive ablation (where the TCO layer was damaged). The optimal performance was achieved at a pulse energy of approximately 37 µJ. At this energy level, the absorber was cleanly ablated, leaving the TCO layer fully exposed and undamaged, which facilitates efficient series interconnection. Module performance was found to degrade at energies both below and above this optimal point, confirming the importance of precise energy control for this step.

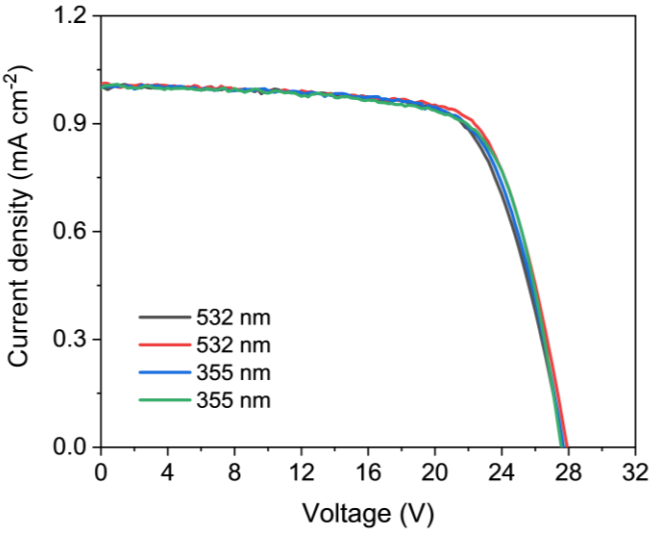

	V_{oc} (V)	J_{sc} (mA cm^{-2})	FF (%)	PCE (%)
532 nm	27.715	1.005	70.1	19.5
532 nm	27.886	1.009	71.8	20.2
355 nm	27.703	1.004	70.7	19.7
355 nm	27.260	0.997	72.3	19.8

Supplementary Figure 52 | J-V curves of all-perovskite TSMs using 532-nm or 355-nm scribing for P2 and P3.

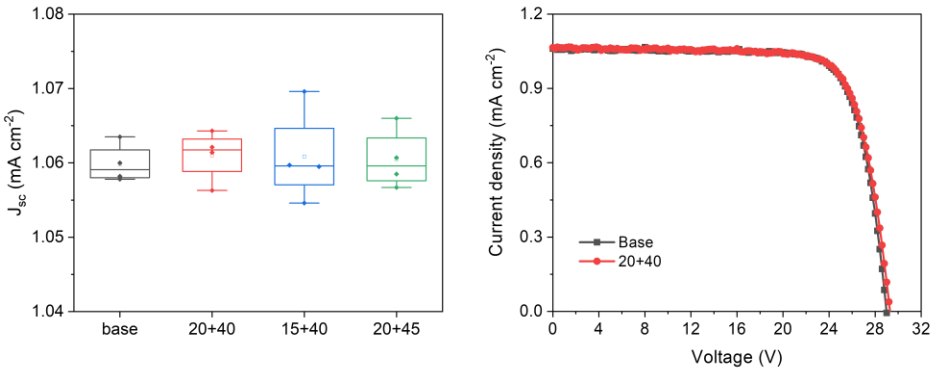

	V_{oc} (V)	J_{sc} (mA cm^{-2})	FF (%)	PCE (%)
Base	28.813	1.063	78.0	23.8
20+40	29.310	1.065	76.9	24.0

Supplementary Figure 53 | Performance of all-perovskite TSMs with P2 and P3 patterning adjusted to reduce the dead area. The notation "20+40" indicates that P2 and P3 are shifted toward P1 by 20 μm and 40 μm, respectively, reducing the dead width from 200 μm to 160 μm. Similarly, "15+40" corresponds to shifts of 15 μm and 40 μm, also achieving a reduction from 200 μm to 160 μm. For "20+45", shifts of 20 μm and 45 μm narrow the dead width from 200 μm to 155 μm.

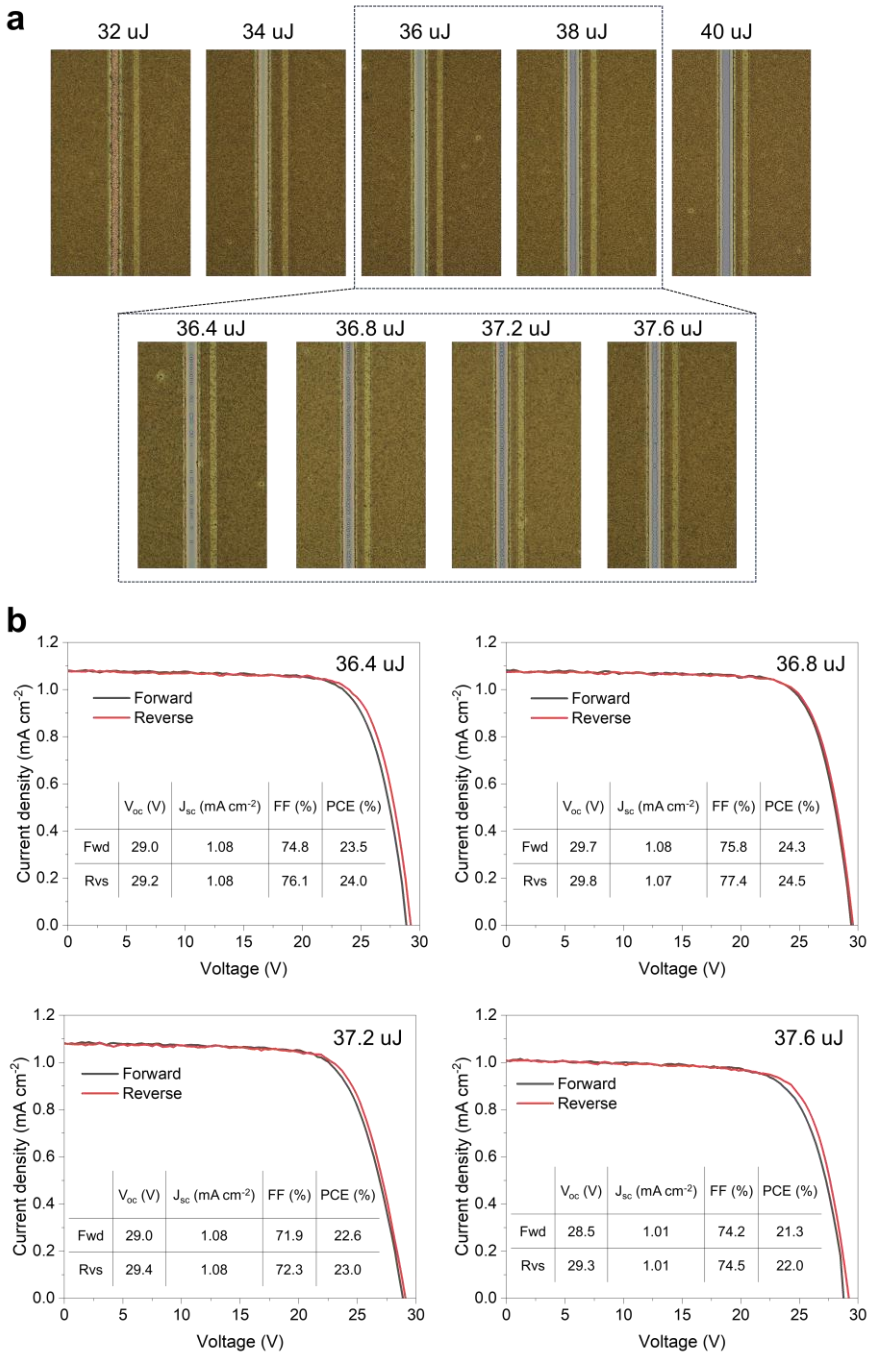

Supplementary Figure 54 | Performance of all-perovskite TSMs with optimized P2 scribing power. (a) Digital photographs showing the effect of P2 laser power variation; (b) J-V characteristics of all-perovskite TSMs fabricated with different P2 scribing powers.

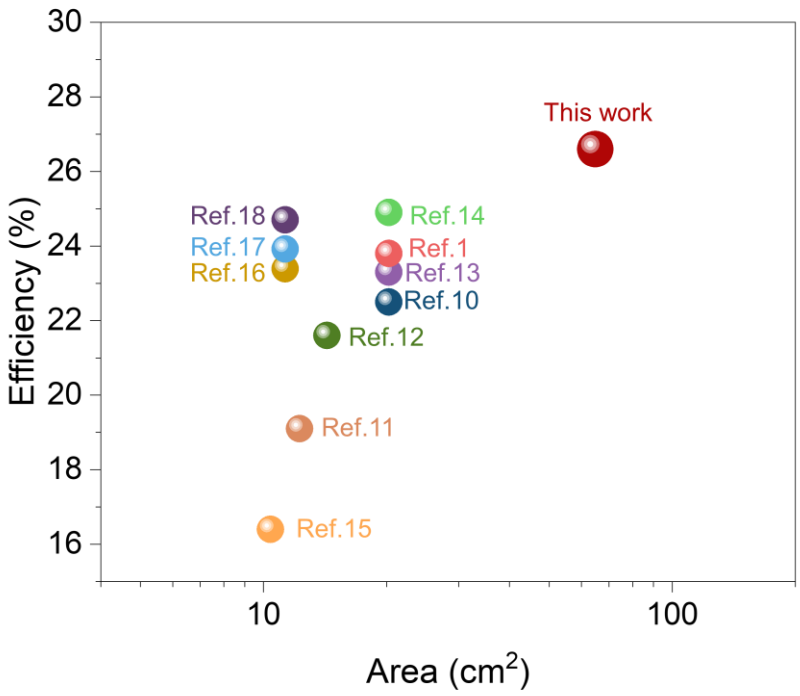

Supplementary Figure 55 | Summary of publicly reported all-perovskite TSMs (aperture area ≥ 10 cm^2).

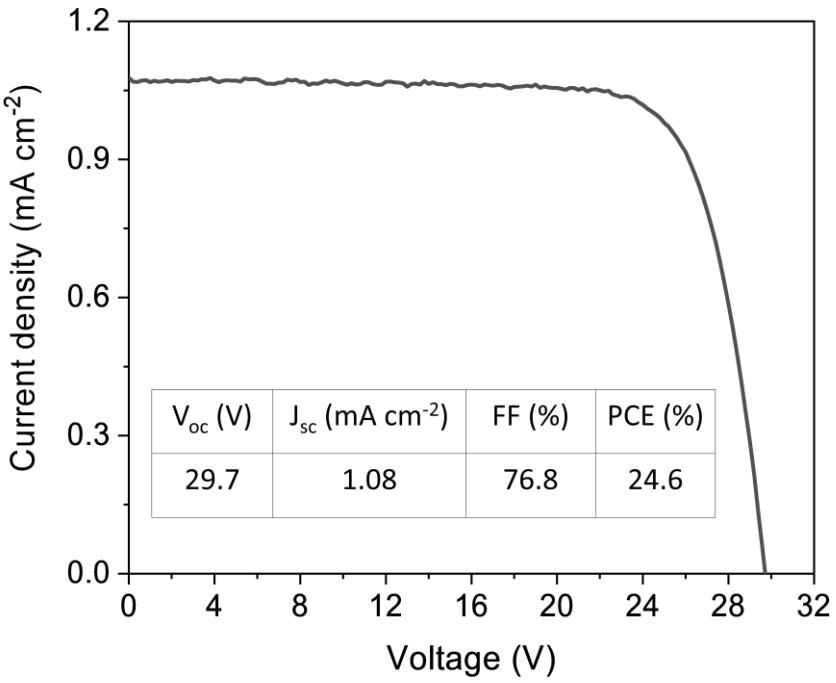

Supplementary Figure 56 | Initial performance of the encapsulated all-perovskite TSM used for MPP tracking.

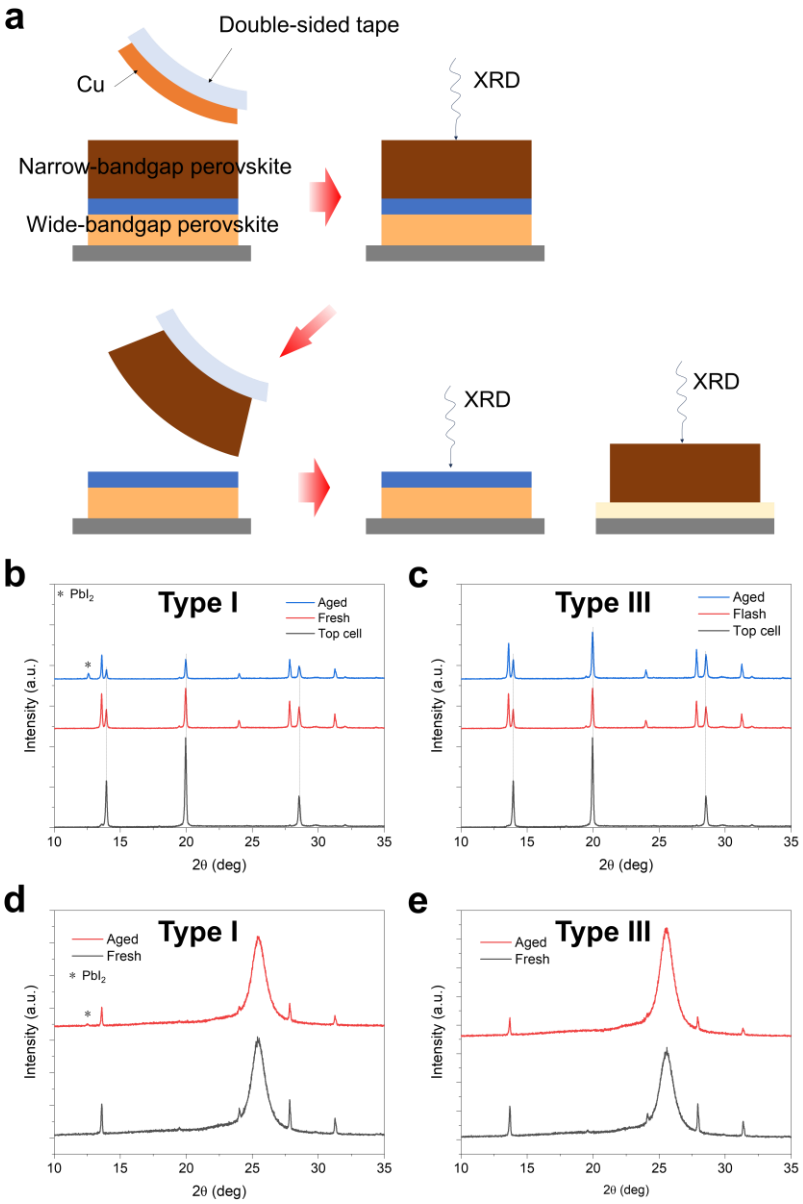

Supplementary Figure 57 | XRD patterns of different structures by peeling off the electrode and Pb-Sn perovskite layer in the TSMs after MPPT tracking. (a) Measured structure of tandem structure with peeled Cu, top cell with peeled Pb-Sn perovskite layer and peeled Pb-Sn perovskite layer attached to the glass substrate; (b and c) XRD patterns of type I (b) and type III (c) with peeled electrode and Pb-Sn perovskite layer before and after MPPT tracking aging; (d and e) XRD patterns of peeled Pb-Sn perovskite layers from type I (d) and type III (e) attached to the glass substrate before and after MPPT tracking aging. The widen peak arises from the attached tape.

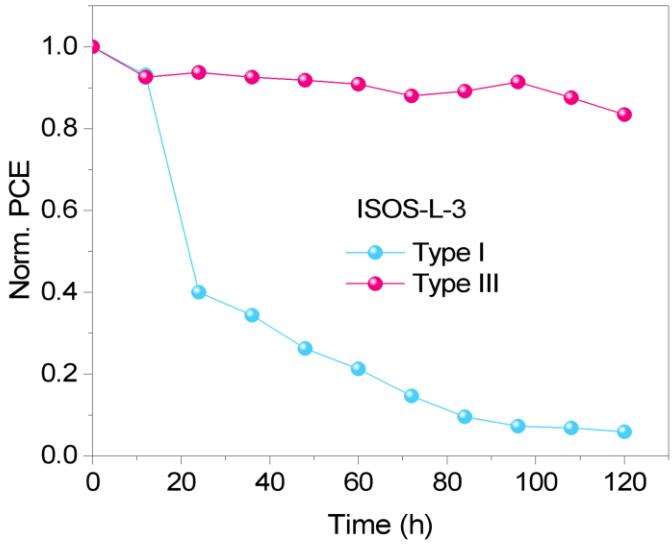

Supplementary Figure 58 | Continuous light soaking of the encapsulated all-perovskite TSM at 65°C condition for 120 hours.

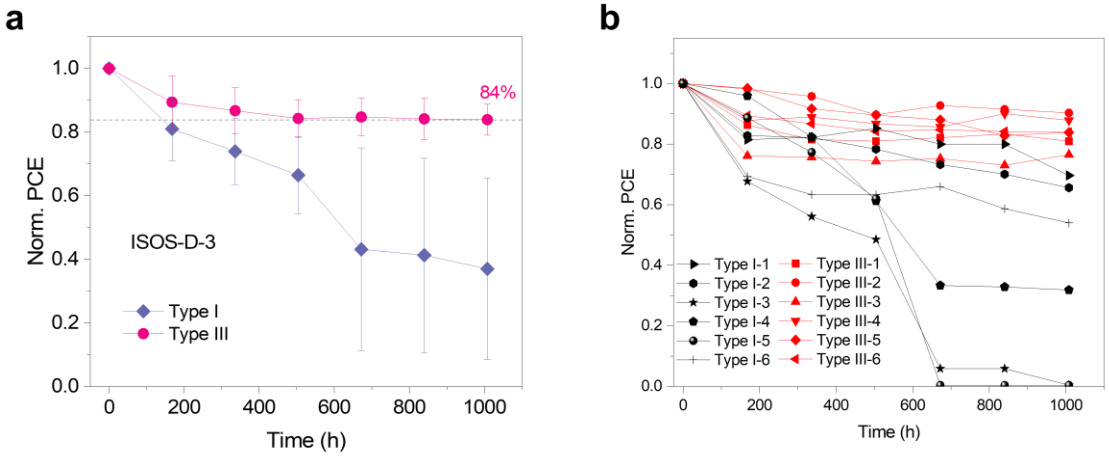

Supplementary Figure 59 | Damp-heat test of all-perovskite TSMs. (a) Normalized averaged PCE of encapsulated type-I and type-III modules under damp-heat test. The error bar represents the PCE standard deviation of the 6 devices for each type. (b) Aging evolution of 6 type-I modules and 6 type-III modules.

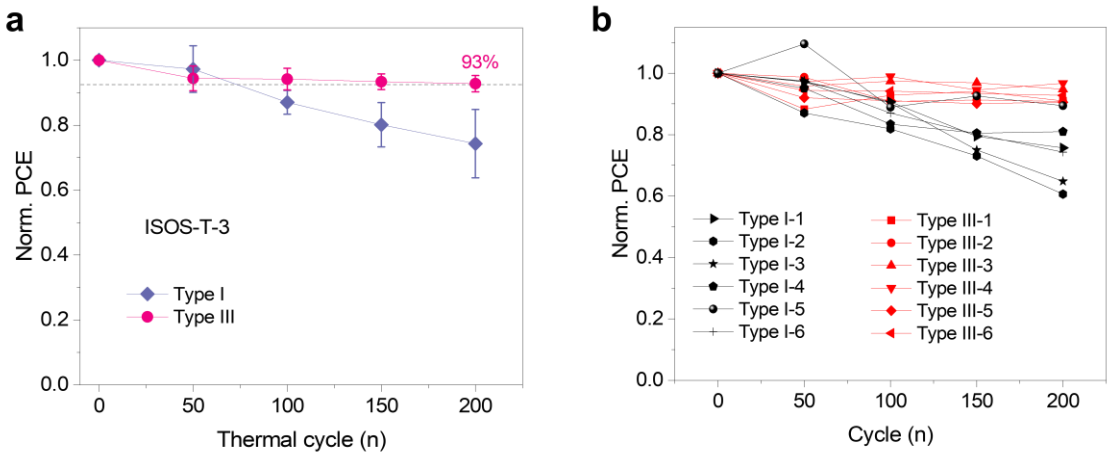

Supplementary Figure 60 | Thermal cycling test of all-perovskite TSMs. (a) Normalized averaged PCE of encapsulated type-I and type-III modules under thermal cycling test. The error bar represents the PCE standard deviation of the 6 devices for each type. (b) Aging evolution of 6 type-I modules and 6 type-III modules.

Supplementary Table 1 The key parameters of the biexponential fitting for the TRPL curves of the control and target perovskite films.

	A_1	τ_1	A_2	τ_2	τ_{ave}
Control	2619.8	308.4	1337.0	1366.3	1041.9
Target	2008.6	507	1842.1	2231.5	1889.1

Supplementary Table 2 Solvent chart with different properties.

	DMF	DMSO	2-Me	THF
Boiling point [°C] at 1 atm	153	189	124.5	65
Vapor pressure [kPa] at 20 °C	0.377	0.055	1.0	17
Evaporation rate n-butyl acetate = 1	0.2	0.026	1	6.3
Gutmann's donor number (DN)	26.6	29.8	19.7	20
Viscosity （mPa.s at 20 °C）	0.86	2.14	1.7	0.456

Supplementary Table 3 Corresponding photovoltaic parameters of the champion control and target Pb-Sn perovskite solar modules shown in Supplementary Fig. 4C.

	V_{oc} (V)	J_{sc} (mA cm^{-2})	FF (%)	PCE (%)
Control-Rev	11.006	2.10	59.8	13.8
Control-Fwd	10.367	2.08	47.1	10.2
Target-Rev	11.724	2.24	75.9	19.9
Target-Fwd	11.572	2.24	76.3	19.8

Supplementary Table 4 Corresponding photovoltaic parameters of the champion type-I and type-III all-perovskite TSMs shown in Fig. 4D.

		V_{oc} (V)	J_{sc} (mA cm^{-2})	FF (%)	PCE (%)
Control	Reverse	29.314	1.093	77.8	24.9
	Forward	29.315	1.091	76.8	24.6
Target	Reverse	30.381	1.121	78.2	26.6
	Forward	29.861	1.119	79.7	26.6

Supplementary Table 5 Summary of publicly reported all-perovskite TSMs (aperture area ≥10 cm^2).

Area (cm^2)	PCE (%) (in-Lab/certified)	V_{OC}(V)	J_{SC} (mA cm^{-2})	FF (%)	Stability	Reference
20.25	22.5/21.7	2.034	14.4	76.8	MPPT: 75%, 500h	Ref [10]
12.25	19.1/-	1.9	14.2	71	MPPT: 93%, 20h	Ref [11]
14.3	21.6/-	2.02	14.0	76.6	MPPT: 90%, 250h	Ref [12]
20.25	23.3/-	2.12	14.3	76.5	MPPT: 80%, 352h	Ref [13]
20.25	23.8/-	2.125	14.56	77.2	MPPT: 75%, 600h	Ref [1]
20.25	24.9/24.5	2.15	14.8	78.2	MPPT (FAMA Pb-Sn): 80%, 330h MPPT (FACs Pb-Sn): 80%, 656h DH200: 80% TC200: 86%	Ref [14]
10.4	16.4/-	1.7	13.8	70	MPPT: 96.3%, 1000s	Ref [15]
11.3	23.39/-	2.04	14.685	78.08	/	Ref [16]
11.3	23.92/-	2.02	14.93	79.29	/	Ref [17]
11.3	24.7/-	2.076	14.835	80.32	MPPT: 80%, 290h	Ref [18]
64.84	26.6/26.2	2.17	15.694	78.2	MPPT: 90%, 771h 82.5%, 1000h DH1000: 84% TC200: 93%	This work

Supplementary references

1. Duan, C. *et al.* Scalable fabrication of wide-bandgap perovskites using green solvents for tandem solar cells. *Nat. Energy* **10**, 318–328 (2024).
2. Boles, M. A., Ling, D., Hyeon, T. & Talapin, D. V. The surface science of nanocrystals. *Nature Materials* vol. 15 141–153 Preprint at https://doi.org/10.1038/nmat4526 (2016).
3. Pai, R. A. & Watkins, J. J. Synthesis of mesoporous organosilicate films in supercritical carbon dioxide. *Advanced Materials* **18**, 241–245 (2006).
4. Xiao, P. *et al.* Ligand-Engineered Direct Optical Lithography of Nanocrystals with Industrially Compatible Solvents. *ACS Nano* **19**, 14509–14520 (2025).
5. Wehrenfennig, C., Eperon, G. E., Johnston, M. B., Snaith, H. J. & Herz, L. M. High Charge Carrier Mobilities and Lifetimes in Organolead Trihalide Perovskites. *Advanced Materials* **26**, 1584–1589 (2014).
6. Tiwana, P., Parkinson, P., Johnston, M. B., Snaith, H. J. & Herz, L. M. Ultrafast Terahertz Conductivity Dynamics in Mesoporous TiO_2 : Influence of Dye Sensitization and Surface Treatment in Solid-State Dye-Sensitized Solar Cells. *The Journal of Physical Chemistry C* **114**, 1365–1371 (2010).
7. La-o-vorakiat, C. *et al.* Elucidating the role of disorder and free-carrier recombination kinetics in CH3NH3PbI3 perovskite films. *Nat. Commun.* **6**, 7903 (2015).
8. Lin, R. *et al.* Monolithic all-perovskite tandem solar cells with 24.8% efficiency exploiting comproportionation to suppress Sn(ii) oxidation in precursor ink. *Nat. Energy* **4**, 864–873 (2019).
9. Lou, J. *et al.* Calibration-free, high-precision, and robust terahertz ultrafast metasurfaces for monitoring gastric cancers. *Proceedings of the National Academy of Sciences* **119**, (2022).
10. Xiao, K. *et al.* Scalable processing for realizing 21.7%-efficient all-perovskite tandem solar modules. *Science (1979).* **376**, 762–767 (2022).
11. Abdollahi Nejand, B. *et al.* Scalable two-terminal all-perovskite tandem solar modules with a 19.1% efficiency. *Nat. Energy* **7**, 620–630 (2022).
12. Dai, X. *et al.* Efficient monolithic all-perovskite tandem solar modules with small cell-to-module derate. *Nat. Energy* **7**, 923–931 (2022).
13. Sun, H. *et al.* Scalable Solution-Processed Hybrid Electron Transport Layers for Efficient All-Perovskite Tandem Solar Modules. *Advanced Materials* **36**, (2024).
14. Gao, H. *et al.* Homogeneous crystallization and buried interface passivation for perovskite tandem solar modules. *Science (1979).* **383**, 855–859 (2024).
15. Shi, Y. *et al.* High-Speed Deposition of Large-Area Narrow-Bandgap Perovskite Films for All-Perovskite Tandem Solar Mini-Modules. *Adv. Funct. Mater.* **33**, 1–8 (2023).
16. Pan, Y. *et al.* Surface chemical polishing and passivation minimize non-radiative recombination for all-perovskite tandem solar cells. *Nat. Commun.* **15**, (2024).
17. Shi, C. *et al.* Modulating competitive adsorption of hybrid self-assembled molecules for efficient wide-bandgap perovskite solar cells and tandems. *Nat. Commun.* **16**, 3029 (2025).
18. Wang, J. *et al.* Mercapto-functionalized scaffold improves perovskite buried interfaces for tandem photovoltaics. *Nature Communications* **16**, (2025).